

Electron Spin Resonance

1. Introduction

Electron spin resonance (ESR) spectroscopy has been used for over 50 years to study a variety of paramagnetic species. Here, we will focus on the spectra of organic and organotransition metal radicals and coordination complexes. Although ESR spectroscopy is supposed to be a mature field with a fully developed theory [1], there have been some surprises as organometallic problems have explored new domains in ESR parameter space. We will start with a synopsis of the fundamentals of ESR spectroscopy. For further details on the theory and practice of ESR spectroscopy, refer to one of the excellent texts on ESR spectroscopy [2-9].

The electron spin resonance spectrum of a free radical or coordination complex with one unpaired electron is the simplest of all forms of spectroscopy. The degeneracy of the electron spin states characterized by the quantum number, $m_S = \pm 1/2$, is lifted by the application of a magnetic field and transitions between the spin levels are induced by radiation of the appropriate frequency, as shown in Figure 1.1. If unpaired electrons in radicals were indistinguishable from free electrons, the only information content of an ESR spectrum would be the integrated intensity, proportional to the radical concentration.

Fortunately, an un-paired electron interacts with its environment, and the details of ESR spectra depend on the nature of those interactions.

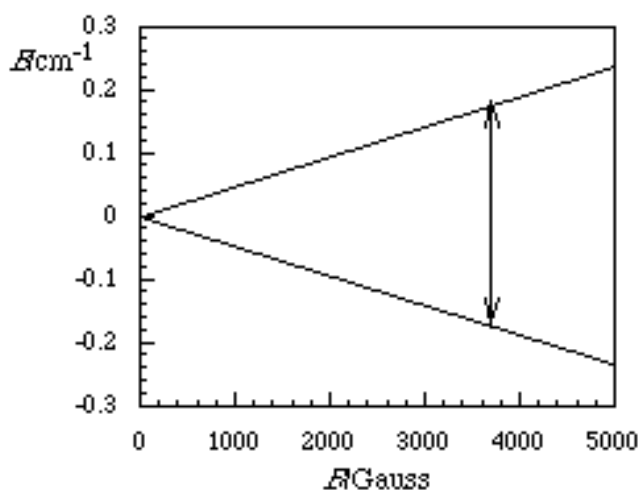


Figure 1.1. Energy levels of an electron placed in a magnetic field. The arrow shows the transitions induced by 0.315 cm^{-1} radiation.

There are two kinds of environmental interactions which are commonly important in the ESR spectrum of a free radical:

1. To the extent that the unpaired electron has unquenched orbital angular momentum, the total magnetic moment is different from the spin-only moment (either larger or smaller, depending on how the angular momentum vectors couple). It is customary to lump the orbital and spin angular

momenta together in an effective spin and to treat the effect as a shift in the energy of the spin transition.

- The electron spin energy levels are split by interaction with nuclear magnetic moments – the nuclear hyperfine interaction. Each nucleus of spin I splits the electron spin levels into $(2I + 1)$ sublevels. Since transitions are observed between sublevels with the same values of m_I , nuclear spin splitting of energy levels is mirrored by splitting of the resonance line.

2. The E.S.R. Experiment

When an electron is placed in a magnetic field, the degeneracy of the electron spin energy levels is lifted as shown in Figure 1 and as described by the **spin Hamiltonian**:

$$\hat{H}_s = g\mu_B B \hat{S}_z \quad (2.1)$$

In eq (2.1), g is called the **g-value** ($g_e = 2.00232$ for a free electron), μ_B is the Bohr magneton (9.274×10^{-28} J G⁻¹), B is the magnetic field strength in Gauss, and \hat{S}_z is the z -component of the spin angular momentum operator (the field defines the z -direction). The electron spin energy levels are easily found by application of the spin Hamiltonian to the electron spin eigenfunctions corresponding to $m_S = \pm 1/2$:

$$\hat{H}_s \left| \pm 1/2 \right\rangle = \pm \frac{1}{2} g\mu_B B \left| \pm 1/2 \right\rangle = E_{\pm} \left| \pm 1/2 \right\rangle$$

Thus

$$E_{\pm} = \pm \frac{1}{2} g\mu_B B \quad (2.2)$$

The difference in energy between the two levels,

$$DE = E_+ - E_- = g\mu_B B$$

corresponds to the energy of a photon required to cause a transition:

$$h\nu = g\mu_B B \quad (2.3)$$

or in wave numbers:

$$\tilde{\nu} = \frac{g\mu_B B}{hc} \quad (2.4)$$

where $g_e\mu_B/hc = 0.9348 \times 10^{-4}$ cm⁻¹G⁻¹. Since the g -values of organic and organometallic free radicals are usually in the range 1.8 - 2.2, the free electron value is a good starting point for describing the experiment.

Magnetic fields of up to ca. 15000 G are easily obtained with an iron-core electromagnet; thus we could use radiation with $\tilde{\nu}$ up to 1.4 cm⁻¹ ($\nu < 42$ GHz or $\lambda > 0.71$ cm). Radiation with this kind of wavelength is in the microwave region. Microwaves are normally handled using waveguides designed to transmit over a

relatively narrow frequency range. Waveguides look like rectangular cross-section pipes with dimensions on the order of the wavelength to be transmitted. As a practical matter, waveguides can't be too big or too small – 1 cm is a bit small and 10 cm a bit large; the most common choice, called X-band microwaves, has l in the range 3.0 - 3.3 cm ($n \sim 9 - 10$ GHz); in the middle of X-band, the free electron resonance is found at 3390 G.

Although X-band is by far the most common, ESR spectrometers are available commercially in several frequency ranges:

Designation	n/GHz	l/cm	$B_{(electron)}/Tesla$
S	3.0	10.0	0.107
X	9.5	3.15	0.339
K	23	1.30	0.82
Q	35	0.86	1.25
W	95	0.315	3.3

Sensitivity

As for any quantum mechanical system interacting with electromagnetic radiation, a photon can induce either absorption or emission. The experiment detects net absorption, *i.e.*, the difference between the number of photons absorbed and the number emitted. Since absorption is proportional to the number of spins in the lower level and emission is proportional to the number of spins in the upper level, net absorption is proportional to the difference:

Net Absorption $\propto N_- - N_+$

The ratio of populations at equilibrium is given by the Boltzmann distribution:

$$\frac{N_+}{N_-} = e^{-\frac{\Delta E}{k_B T}} = e^{-\frac{g\mu_B B}{k_B T}} \quad (2.5)$$

For ordinary temperatures and ordinary magnetic fields, the exponent is very small and the exponential can be accurately approximated by the expansion, $e^{-x} \sim 1 - x$. Thus:

$$\frac{N_+}{N_-} = 1 - \frac{g\mu_B B}{k_B T}$$

Since $N_- \sim N_+ \sim N/2$, the population difference can be written

$$N_- - N_+ = N_- \left[1 - \left(1 - \frac{g\mu_B B}{k_B T} \right) \right] = \frac{N g \mu_B B}{2 k_B T} \quad (2.6)$$

This expression tells us that ESR sensitivity (net absorption) increases with decreasing temperature and with increasing magnetic field strength. Since field is proportional to microwave frequency, in principle sensitivity should be greater for K-band or Q-band or W-band spectrometers than for X-band. However, since the K-, Q- or W-band waveguides are smaller, samples are also necessarily smaller, usually more than canceling the advantage of a more favorable Boltzmann factor.

Under ideal conditions, a commercial X-band spectrometer can detect the order of 10^{12} spins (10^{-12} moles) at room temperature. By ideal conditions, we mean a single line, on the order of 0.1 G wide; sensitivity goes down roughly as the reciprocal square of the linewidth. When the resonance is split into two or more hyperfine lines, sensitivity goes down still further. Nonetheless, ESR is a remarkably sensitive technique, especially compared with NMR.

Saturation

Because the two spin levels are so nearly equally populated, magnetic resonance suffers from a problem not encountered in higher energy forms of spectroscopy: An intense radiation field will tend to equalize the populations, leading to a decrease in net absorption; this effect is called "saturation". A spin system returns to thermal equilibrium via energy transfer to the surroundings, a rate process called **spin-lattice relaxation**, with a characteristic time, T_1 , the spin-lattice relaxation time (rate constant = $1/T_1$). Systems with a long T_1 (i.e., spin systems weakly coupled to the surroundings) will be easily saturated; those with shorter T_1 will be more difficult to saturate. Since spin-orbit coupling provides an important energy transfer mechanism, we usually find that odd-electron species with light atoms (*e.g.*, organic radicals) have long T_1 's, those with heavier atoms (*e.g.*, organotransition metal radicals) have shorter T_1 's. The effect of saturation is considered in more detail in [Appendix I](#), where the phenomenological Bloch equations are introduced.

Nuclear Hyperfine Interaction

When one or more magnetic nuclei interact with the unpaired electron, we have another perturbation of the electron energy, *i.e.*, another term in the spin Hamiltonian:

$$\hat{H}_s = g\mu_B B \hat{S}_z + A \vec{I} \cdot \vec{S} \quad (2.7)$$

(Strictly speaking we should include the nuclear Zeeman interaction, gBI_z . However, in most cases the energy contributions are negligible on the ESR energy scale, and, since observed transitions are between levels with the same values of m_I , the nuclear Zeeman energies cancel in computing ESR transition energies.) Expanding the dot product and substituting the raising and lowering operators for S_x , S_y , I_x , and I_y ($\hat{S}_x = \hat{S}_+ \pm i\hat{S}_-$, $\hat{I}_x = \hat{I}_+ \pm i\hat{I}_-$), we have

$$\hat{H}_r = g\mu_B B \hat{S}_z + A \hat{I}_z \hat{S}_z + \frac{1}{2} (\hat{I}_+ \hat{S}_- + \hat{I}_- \hat{S}_+) \quad (2.8)$$

Suppose that the nuclear spin is 1/2; operating on the spin functions, $|m_S, m_I\rangle$ we get:

$$\hat{H}_r |1/2, 1/2\rangle = \left(\frac{1}{2} g\mu_B B + \frac{1}{4} A\right) |1/2, 1/2\rangle$$

$$\hat{H}_r |1/2, -1/2\rangle = \left(\frac{1}{2} g\mu_B B - \frac{1}{4} A\right) |1/2, -1/2\rangle + \frac{1}{2} A |1/2, 1/2\rangle$$

$$\hat{H}_r |-1/2, 1/2\rangle = \left(-\frac{1}{2} g\mu_B B - \frac{1}{4} A\right) |-1/2, 1/2\rangle + \frac{1}{2} A |1/2, -1/2\rangle$$

$$\hat{H}_r |-1/2, -1/2\rangle = \left(-\frac{1}{2} g\mu_B B + \frac{1}{4} A\right) |-1/2, -1/2\rangle$$

The Hamiltonian matrix thus is

$$\begin{pmatrix} \frac{1}{2} g\mu_B B + \frac{1}{4} A & 0 & 0 & 0 \\ 0 & \frac{1}{2} g\mu_B B - \frac{1}{4} A & \frac{1}{2} A & 0 \\ 0 & \frac{1}{2} A & -\frac{1}{2} g\mu_B B - \frac{1}{4} A & 0 \\ 0 & 0 & 0 & -\frac{1}{2} g\mu_B B + \frac{1}{4} A \end{pmatrix} \quad (2.9)$$

If the hyperfine coupling is sufficiently small, $A \ll g\mu_B B$, the diagonal elements, which correspond to the energies to first-order in perturbation theory, will be sufficiently accurate:

$$E = \pm \frac{1}{2} g\mu_B B \pm \frac{1}{4} A \quad (2.10)$$

However, for large A, the matrix must be diagonalized. This is easy when there is only one hyperfine coupling:

$$E(1/2, 1/2) = \frac{1}{2} g\mu_B B + \frac{1}{4} A \quad (2.11a)$$

$$E(1/2, -1/2) = -\frac{1}{2} g\mu_B B + \frac{1}{4} A \quad (2.11b)$$

$$E(1/2, -1/2) = -\frac{1}{4} A + \frac{1}{2} g\mu_B B \sqrt{1 + \left(\frac{A}{g\mu_B B}\right)^2} \quad (2.11c)$$

$$E(-1/2, 1/2) = -\frac{1}{4} A - \frac{1}{2} g\mu_B B \sqrt{1 + \left(\frac{A}{g\mu_B B}\right)^2} \quad (2.11d)$$

These equations are a special case of the general solution to eq (2.8), called the **Breit-Rabi equation** (10).

The energies are plotted as functions of B in Figure 2.1 for $g = 2.00$, $A = 0.1 \text{ cm}^{-1}$. Notice that at zero

field, there are two levels corresponding to a spin singlet ($E = -3A/4$) and a triplet ($E = +A/4$).

At high field, the four levels divide into two higher levels ($m_S = +1/2$) and two lower levels ($m_S = -1/2$) and approach the first-order results, eq (2.10) (the first-order solution is called the high-field approximation). In order to conserve angular momentum, transitions among these levels can involve only one spin flip; in other words, the selection rules are $\Delta m_S = \pm 1$, $\Delta m_I = 0$ (ESR transitions) or $\Delta m_S = 0$, $\Delta m_I = \pm 1$ (NMR transitions); the latter involves much lower energy photons, and, in practice, only the $\Delta m_S = \pm 1$ transitions are observed. In Figure 2.1, these transitions are marked for a photon energy of 0.315 cm^{-1} .

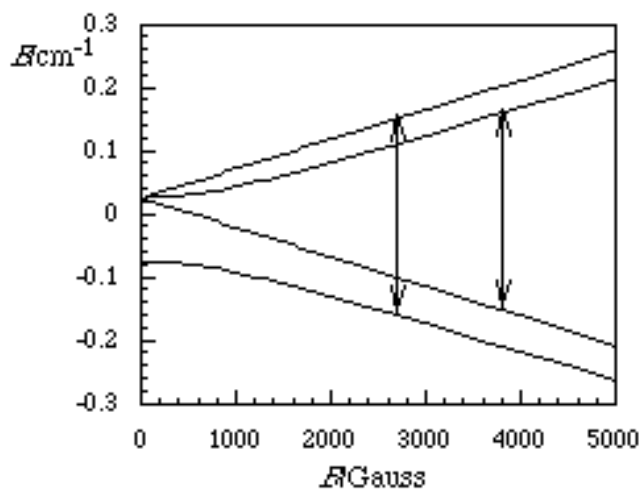


Figure 2.1. Energy levels for an electron interacting with a spin 1/2 nucleus, $g = 2.00$, $A = 0.10 \text{ cm}^{-1}$. The arrows show the transitions induced by 0.315 cm^{-1} radiation.

3. Operation of an ESR Spectrometer

Although many spectrometer designs have been produced over the years, the vast majority of laboratory instruments are based on the simplified block diagram shown in Figure 3.1.

Microwaves are generated by the Klystron tube and the power level adjusted with the Attenuator. The Circulator behaves like a traffic circle: microwaves entering from the Klystron are routed toward the Cavity where the sample is mounted.

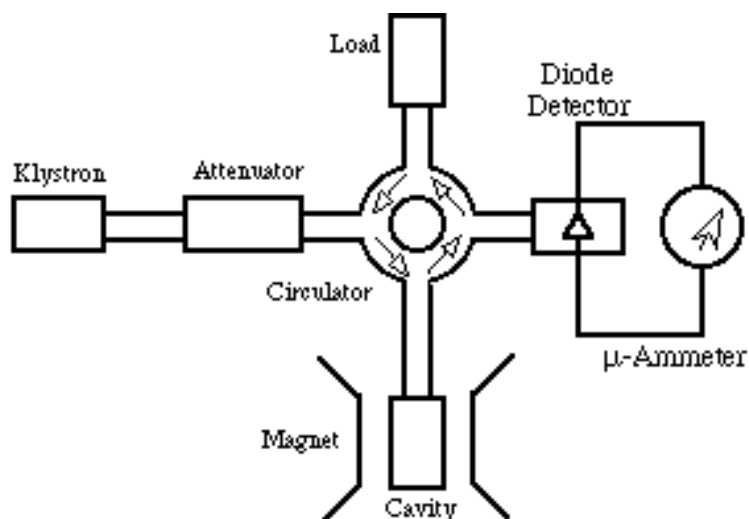


Figure 3.1. Block diagram of an ESR spectrometer.

Microwaves reflected back from the cavity (less when power is being absorbed) are routed to the diode detector, and any power reflected from the diode is absorbed completely by the Load. The diode is mounted along the E -vector of the plane-polarized microwaves and thus produces a current proportional to the microwave power reflected from the cavity. Thus, in principle, the absorption of microwaves by the sample could be detected by noting a decrease in current in the microammeter. In practice, of course, such a d.c. measurement would be far too noisy to be useful.

The solution to the signal-to-noise ratio problem is to introduce small amplitude field modulation. An oscillating magnetic field is super-imposed on the d.c. field by means of small coils, usually built into the cavity walls. When the field is in the vicinity of a resonance line, it is swept back and forth through part of the line, leading to an a.c. component in the diode current. This a.c. component is amplified using a frequency selective amplifier, thus eliminating a great deal of noise. The modulation amplitude is normally less than the line width. Thus the detected a.c. signal is proportional to the *change* in sample absorption. As shown in Figure 3.2, this amounts to detection of the first derivative of the absorption curve

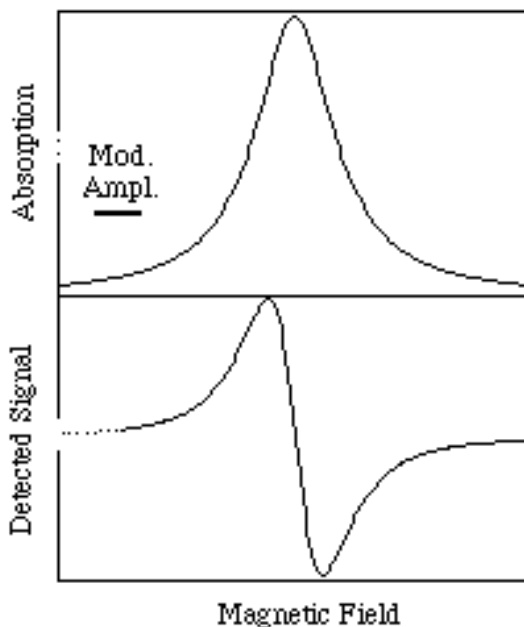


Figure 3.2. Small-amplitude field modulation converts absorption curve to first-derivative.

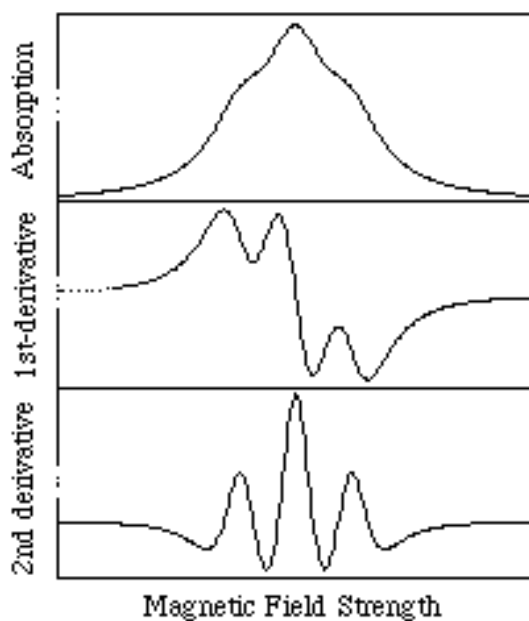


Figure 3.3. First-derivative curves show better apparent resolution than do absorption curves.

It takes a little practice to get used to looking at first-derivative spectra, but there is a distinct advantage: first-derivative spectra have much better apparent resolution than do absorption spectra. Indeed, second-derivative spectra are even better resolved (though the signal-to-noise ratio decreases on further differentiation).

The microwave-generating klystron tube requires a bit of explanation. A schematic drawing of the klystron is shown in Figure 3.3. There are three electrodes: a heated cathode from which electrons are emitted, an anode to collect the electrons, and a highly negative reflector electrode which sends those electrons which pass through a hole in the anode back to the anode.

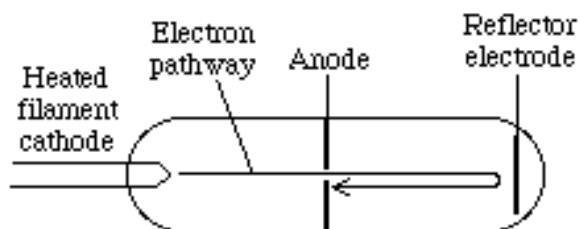


Figure 3.3. Schematic drawing of a microwave-generating klystron tube.

The motion of the charged electrons from the hole in the anode to the reflector and back to the anode generates an oscillating electric field and thus electromagnetic radiation. The transit time from the hole to the reflector and back again corresponds to the period of oscillation ($1/n$). Thus the microwave frequency can be tuned (over a small range) by adjusting the physical distance between the anode and the reflector or by adjusting the reflector voltage. In practice, both methods are used: the metal tube is distorted mechanically to adjust the distance (a coarse frequency adjustment) and the reflector voltage is adjusted as a fine control.

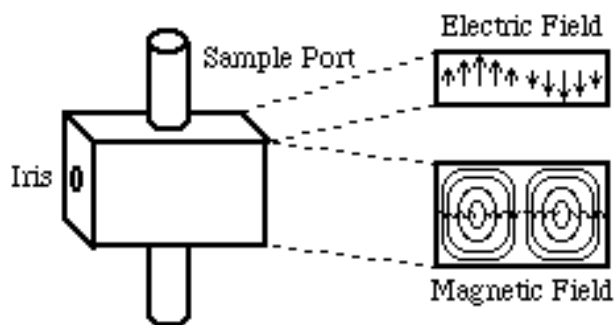


Figure 3.4. Microwave cavity.

The sample is mounted in the microwave cavity, shown in Figure 3.4. The cavity is a rectangular metal box, exactly one wavelength in length. An X-band cavity has dimensions of about $1 \times 2 \times 3$ cm. The electric and magnetic fields of the standing wave are shown in the figure. Note that the sample is mounted in the electric field nodal plane, but at a maximum in the magnetic field.

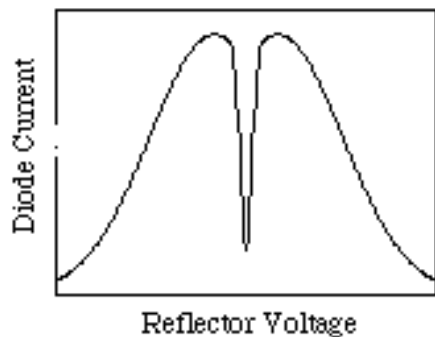


Figure 3.5. Klystron mode and cavity dip.

Since the cavity length is not adjustable but it must be exactly one wavelength, the spectrometer must be tuned such that the klystron frequency is equal to the cavity resonant frequency. The tune-up procedure usually includes observing the klystron power mode. That is, the klystron reflector voltage is swept, and the diode current is plotted on an oscilloscope or other device. When the klystron frequency is close to the

cavity resonant frequency, much less power is reflected from the cavity to the diode, resulting in a dip in the power mode as shown in Figure 3.5. The "cavity dip" is centered on the power mode using the coarse mechanical frequency adjustment with the reflector voltage used to fine tune the frequency.

4. Isotropic ESR Spectra

An isotropic ESR spectrum; the spectrum of a freely tumbling radical in liquid solution; can contain several kinds of chemically useful information:

1. The hyperfine coupling pattern provides information on the numbers and kinds of magnetic nuclei with which the unpaired electron interacts.
2. The spacing of the lines and the center of gravity of the spectrum yield the hyperfine coupling constants, $\langle A_S \rangle$ and g -value, $\langle g \rangle$, which are related to the way in which the unpaired electron spin density is distributed in the molecule.
3. The integrated intensity of the spectrum is proportional to the concentration of radicals in the sample.
4. The spectral linewidths are related to the rate of the rotational motions which average anisotropies in the g - and hyperfine matrices (see §5) and to the rates of fluxional processes which average nuclear positions in a radical.
5. The saturation behavior of a spectrum – the variation of integrated intensity with microwave power – is related to the spin-lattice relaxation time, a measure of the rate of energy transfer between the electron spin and its surroundings.

The degree to which these kinds of information have been exploited varies widely. Although experimentalists often make qualitative observations relating "strong" or "weak" spectra to chemical circumstances, quantitative applications of integrated intensities are rare in ESR studies. This could be a useful analytical approach in some cases. The interested reader is referred to Wertz and Bolton [5], who discuss the technique, point out the variables which must be controlled, and suggest intensity standards.

Largely because spin-orbit coupling results in spin state admixture, electronic spin-lattice relaxation times are normally short for species containing heavy atoms such as transition metals. This has two consequences. Short relaxation times mean that saturation problems, which plague ESR spectroscopists studying organic radicals and NMR spectroscopists in general, are largely absent in organometallic ESR studies. Thus spectra ordinarily can be recorded at full microwave power with salutary consequences for sensitivity. On the other hand, relaxation times are most easily determined by measuring spectral intensity as a function of microwave power in the saturation region. If relaxation times are short, very high power is required, out of the range of operation of most spectrometers.

Line Positions in Isotropic Spectra

ESR spectra of radicals in liquid solution are usually interpreted in terms of a spin Hamiltonian

$$\hat{H}_r = \mu_B \langle g \rangle \vec{B} \cdot \vec{S} + \sum_i \langle A_i \rangle \vec{I}_i \cdot \vec{S} \quad (4.1)$$

where μ_B is the Bohr magneton. The first term of eq (4.1) represents the Zeeman interaction of the effective electron spin, \vec{S} , and the applied magnetic field, \vec{B} , and the second represents the nuclear hyperfine interaction of \vec{S} and the nuclear spins, \vec{I}_i . The spectral information is contained in the parameters, $\langle g \rangle$, the effective gyromagnetic ratio or g -value, and $\langle A_i \rangle$, the electron-nuclear hyperfine

coupling constant for nucleus i . Using spin functions based on the quantum numbers m_S and m_i , eq (4.1) can be used to compute energy levels. Equating energy differences for the allowed transitions ($\Delta m_S = \pm 1$, $\Delta m_i = 0$) with the microwave photon energy,

$$E(m_S = 1/2) - E(m_S = -1/2) = h\nu \quad (4.2)$$

the resonant magnetic field can be predicted. To first-order in perturbation theory, the resonant field is

$$B = B_0 - \sum_i \langle a_i \rangle m_i \quad (4.3)$$

where $B_0 = h\nu / \langle g \rangle \mu_B$ represents the center of the spectrum and $\langle a_i \rangle = \langle A_S \rangle / \langle g \rangle \mu_B$ is the hyperfine coupling constant in field units.

The coupling constant in eq(4.1) has energy units, but the energies are very small so that frequency (MHz) or wave number (10^{-4} cm^{-1}) units are more commonly used. Even more often, however, isotropic coupling constants are given in units of magnetic field strength, usually gauss, though SI purists sometimes use millitesla ($1 \text{ mT} = 10 \text{ G}$). Conversions from units of gauss to frequency or wave number units involves the g -value

$$\langle A \rangle / \text{MHz} = 2.8025 (\langle g \rangle / g_e) \langle a \rangle / \text{G} \quad (4.4a)$$

$$\langle A \rangle / 10^{-4} \text{ cm}^{-1} = 0.93480 (\langle g \rangle / g_e) \langle a \rangle / \text{G} \quad (4.4b)$$

Note that coupling constants in 10^{-4} cm^{-1} are comparable in magnitude to those expressed in gauss. Although the units used for isotropic hyperfine coupling constants is largely a matter of taste, the components of an anisotropic hyperfine coupling matrix (see §5) should be given in frequency or wave number units unless the g -matrix is virtually isotropic

[\(continued\)](#)

Hyperfine Coupling Patterns

Nuclear hyperfine coupling results in a multi-line ESR spectrum, analogous to the spin-spin coupling multiplets of NMR spectra. ESR spectra are simpler to understand than NMR spectra in that second-order effects normally do not alter the intensities of components; on the other hand, ESR multiplets can be much more complex when the electron interacts with several high-spin nuclei, and, as we will see below, there can be considerable variation in linewidth within a spectrum.

When several magnetically equivalent nuclei are present in a radical, some of the multiplet lines are degenerate, resulting in variations in component intensity. Equivalent spin 1/2 nuclei such as ^1H , ^{19}F , or ^{31}P result in multiplets with intensities given by binomial coefficients (1:1 for two nuclei, 1:2:1 for two, 1:3:3:1 for three, 1:4:6:4:1 for four, etc.). One of the first aromatic organic radical anions studied by ESR spectroscopy was the naphthalene anion [[11](#)], the spectrum of which is shown in Figure 4.1. The spectrum consists of 25 lines, a quintet of quintets as expected for hyperfine coupling to two sets of four equivalent protons.

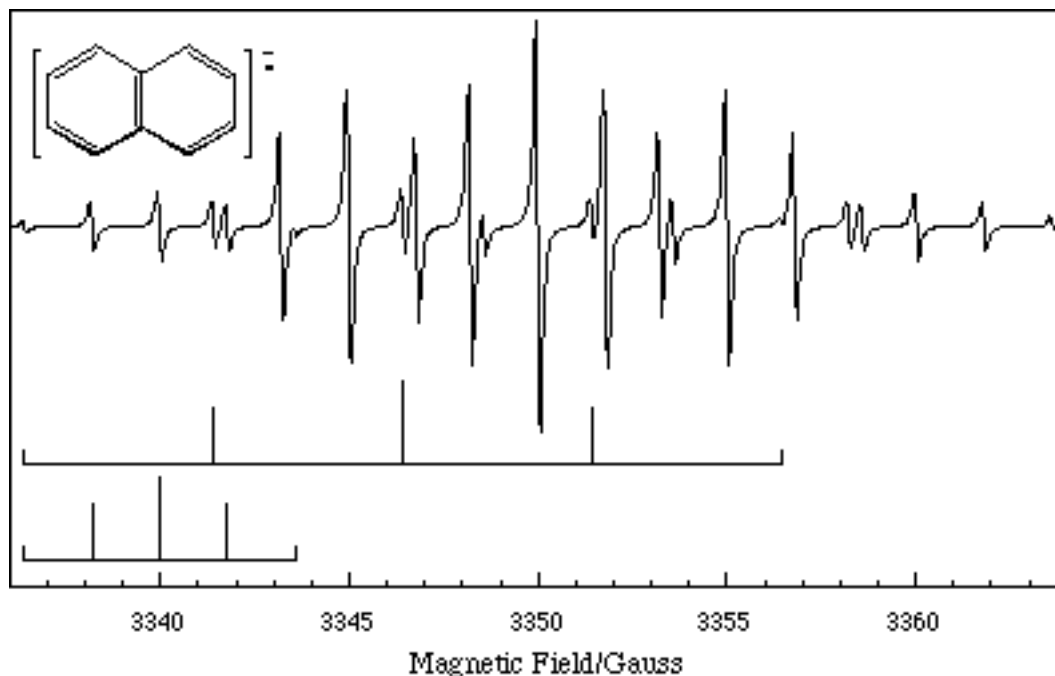


Figure 4.1. ESR spectrum of the naphthalene anion radical (From Reference [11](#)); stick spectra at the bottom show the 1:4:6:4:1 quintets corresponding to coupling to the two sets of four equivalent protons.

The naphthalene anion radical spectrum provided a number of surprises. It was a surprise at the time that such an odd-electron species would be stable, but in the absence of air or other oxidants, $[\text{C}_{10}\text{H}_8]^-$ is stable virtually indefinitely. A second surprise was the appearance of hyperfine coupling to the protons. The odd electron was presumed (correctly) to occupy a p^* MO with the protons in the nodal plane. The mechanism of coupling (discussed below) requires "contact" between the unpaired electron and the proton, an apparent impossibility. A third surprise was the ratio of the magnitudes of the two couplings, $5.01 \text{ G}/1.79 \text{ G} = 2.80$. This ratio is in surprising agreement with the ratio of charge densities predicted for the lowest unoccupied MO (LUMO) at the a and b positions by simple Hückel MO theory, 2.62. This result led to Hückel MO theory being used extensively in the semi-quantitative interpretation of ESR spectra of aromatic radicals.

Just as in NMR, a multiplet pattern gives an important clue to the identity of a radical. For example, the series of radicals derived from the nucleophilic displacement of $\text{Co}(\text{CO})_4^-$ from $[(\text{RCCR}')\text{Co}_2(\text{CO})_6]^-$ by CO, phosphines, or phosphites was identified in large part from the resulting hyperfine patterns [12].

Depending on the nucleophile, spectra were observed which showed coupling to 0, 1, 2, or 3 ^{31}P nuclei, but always to a single ^{59}Co nucleus. The parameters $\langle g \rangle$ and a^{Co} were found to depend slightly on the substituents on the acetylene moiety, suggesting that the acetylene was retained in the radical, but otherwise the parameters were nearly constant over the series, suggesting a single family of radicals. The appearance of 0 - 3 phosphorus couplings suggested three additional ligands, either CO or a phosphine or phosphite. Taken together, this information identified the radicals as $(\text{RCCR}')\text{CoL}_3$, where $\text{L} = \text{CO}$, PR_3 , or $\text{P}(\text{OR})_3$. Figure 4.2(a) shows the experimental first-derivative spectrum of $(\text{Ph}_2\text{C}_2)\text{Co}(\text{CO})_2\text{P}(\text{OMe})_3$, **1**, and Figure 4.2(c) shows a first-order "stick spectrum" showing the line positions ($\langle g \rangle = 2.061$, $a^{\text{Co}} = 45.2 \text{ G}$, $a^{\text{P}} = 176.2 \text{ G}$). Hyperfine coupling to ^{59}Co ($I = 7/2$) and ^{31}P ($I = 1/2$) nuclei results in an octet of doublets. The spectrum is somewhat complicated by the obvious variation in linewidth, but the assignments are quite straightforward.

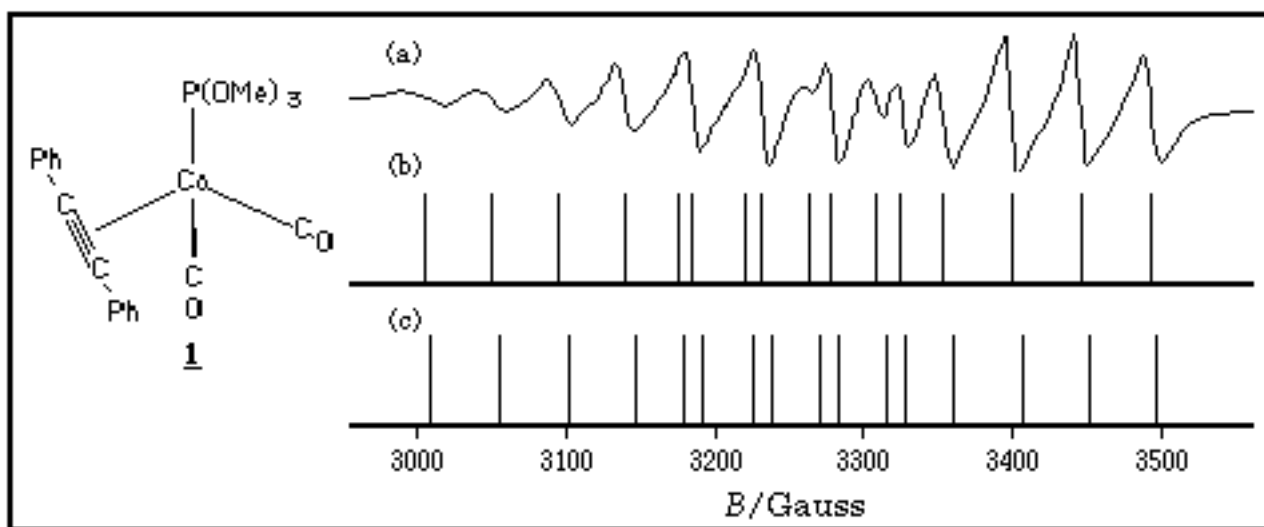


Figure 4.2. (a) Isotropic ESR spectrum of $(\text{Ph}_2\text{C}_2)\text{Co}(\text{CO})_2\text{P}(\text{OMe})_3$ (**1**) in THF solution at 260 K (from reference 12); (b) Second-order "stick spectrum"; (c) First-order "stick spectrum".

Nuclei with $I > 1/2$ give less familiar multiplet intensity ratios. Thus, for example, three equivalent ^{59}Co nuclei ($I = 7/2$) give (to first order) 22 lines with intensity ratios 1:3:6:10:15:21:28:36:42:46:48:48:46:42:36:28:21:15:10:6:3:1, as shown in Figure 4.3(a). The experimental spectrum of $[\text{PhCCo}_3(\text{CO})_9]^-$, **2** [13], which shows this coupling pattern, is given in Figure 4.3(c).

Spin Hamiltonian Parameters from Spectra

Once a hyperfine pattern has been recognized, the line position information can be summarized by the spin Hamiltonian parameters, $\langle g \rangle$ and $\langle a \rangle$. These parameters can be extracted from spectra by a linear least-squares fit of experimental line positions to eq (4.3). However, for high-spin nuclei and/or large couplings, one soon finds that the lines are not evenly spaced as predicted by eq (4.3) and second-order corrections must be made. Solving the spin Hamiltonian, eq (4.1), to second order in perturbation theory, eq (4.3) becomes

$$B = B_0 - \sum_i \left\{ \left(a_i \right) m_i + \left[\left(a_i \right)^2 / 2B \right] \left[I_i(I_i + 1) - m_i^2 \right] + \dots \right\} \quad (4.5)$$

The magnitude of the second-order corrections is often quite significant. For example, [Figure 4.2\(b\)](#) shows a stick spectrum computed to second-order for **1**. Notice that all lines are shifted to low field, relative to the first-order spectrum, but, as expected from eq (4.5), the shift depends on m_{Co} . Failure to account for the second-order terms in an analysis results in a significant error in both the g -value and in the hyperfine coupling constants. For large I_i and a , well-resolved spectra may warrant inclusion of third- or higher-order corrections. Since the third-order corrections involve cross terms among coupling constants, in principle they permit determination of the relative signs of the coupling constants. However, in the example of [Figure 4.2](#), the third-order corrections amount to *ca.* 0.1 - 0.2 G, too small to be significant given the resolution of the experimental spectrum. When coupling constants are really large, it is better to fit line positions to the exact energy levels given by the Breit-Rabi equation [[10,14](#)].

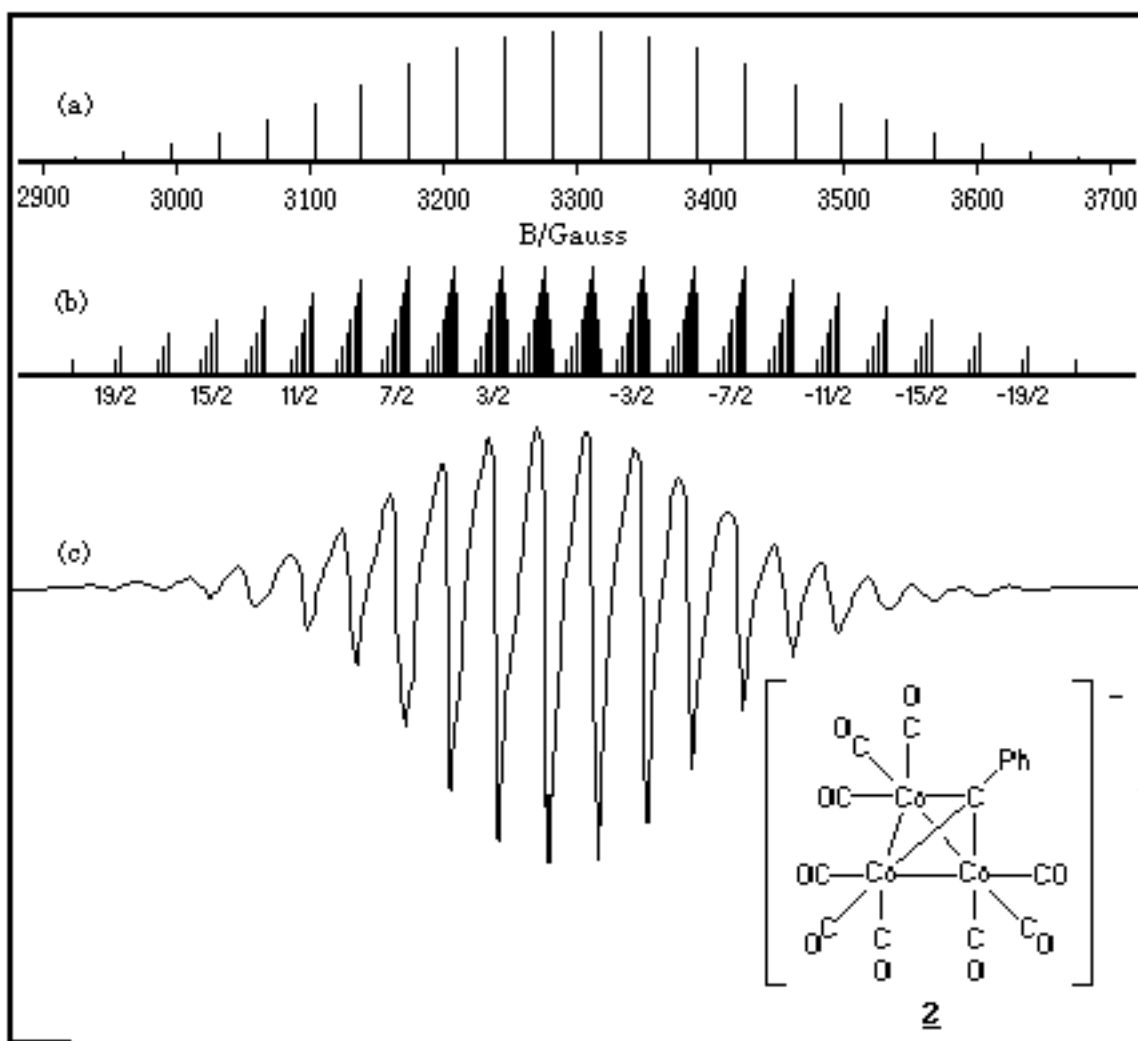


Figure 4.3. "Stick spectrum" showing hyperfine pattern for coupling to three equivalent ^{59}Co nuclei ($I = 7/2$) computed to (a) first-order and (b) second-order in perturbation theory; (c) Isotropic ESR spectrum of $[\text{PhCCo}_3(\text{CO})_9]^-$ in THF solution at 40°C (from reference [13](#)).

Second Order Splittings

Equation (4.5) describes line positions correctly for spectra with hyperfine coupling to two or more nuclei provided that the nuclei are not magnetically equivalent. When two or more nuclei are completely equivalent, *i.e.*, both instantaneously equivalent and equivalent over a time average, then the nuclear spins should be described in terms of the total nuclear spin quantum numbers J and m_J rather than the individual I_i and m_i . In this "coupled representation", the degeneracies of some multiplet lines are lifted when second-order shifts are included. This can lead to extra lines and/or asymmetric line shapes. The effect was first observed in the spectrum of the methyl radical, CH_3 . The three equivalent protons lead to a nondegenerate nuclear spin state with $J = 3/2$ ($m = \pm 3/2, \pm 1/2$) and a two-fold degenerate state with $J = 1/2$ ($m = \pm 1/2$). Thus six hyperfine lines are observed under conditions of high resolution, as shown in Figure 4.4

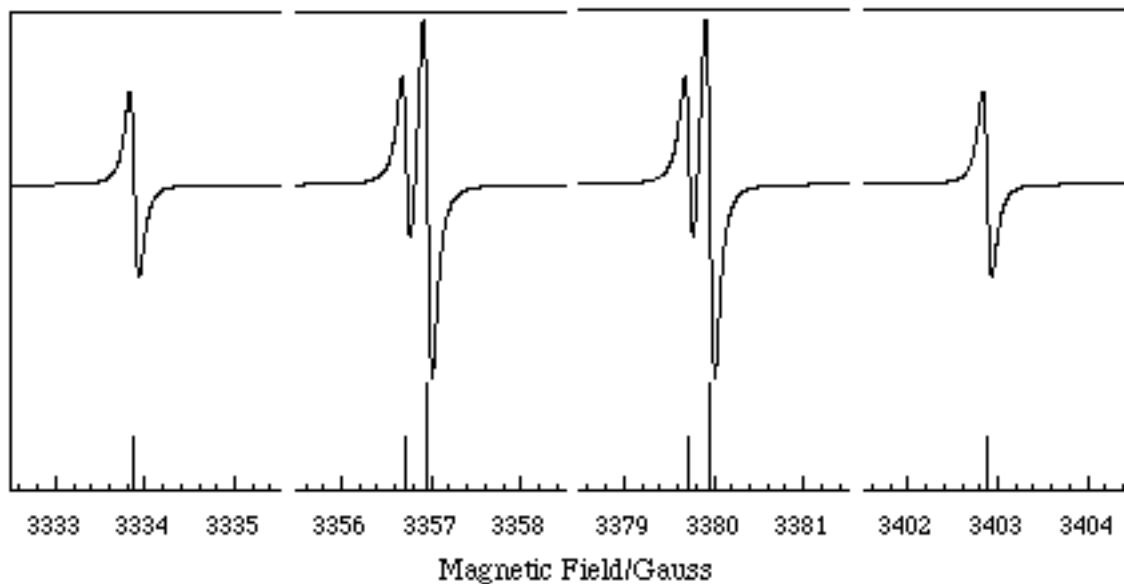


Figure 4.4. ESR spectrum of the methyl radical, CH_3 (from reference [15](#); note discontinuities in magnetic field axis).

Another example is the spectrum of a tricobaltcarbon radical anion, where the three equivalent spin $7/2$ ^{59}Co nuclei should be described in terms of 11 J -states with J ranging from $21/2$ to $1/2$. The $m_J = 17/2$ feature, for example, has three components with $J = 21/2, 19/2,$ and $17/2$, degeneracies of 1, 2, and 3, and second-order shifts of $97 \langle a \rangle^2/4B, 55 \langle a \rangle^2/4B,$ and $17 \langle a \rangle^2/4B$, respectively. The shifts are too small to be resolved, but they lead to an asymmetric absorption line envelope with apparent broadening on the low-field side, as shown in [Figure 4.3\(a\)](#) and as is observed in the experimental spectrum of **2**, shown in [Figure 4.3\(c\)](#) [[13](#)].

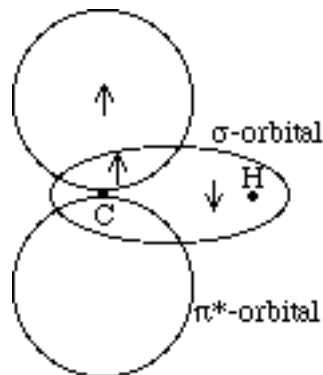
Interpretation of Isotropic Parameters

When ESR spectra were obtained for the benzene anion radical, $[\text{C}_6\text{H}_6]^-$, and the methyl radical, CH_3 , the proton hyperfine coupling constants were found to be 3.75 G and 23.0 G, respectively. Since each carbon atom of the benzene anion carries an electron spin density of $1/6$, the two results suggest that the proton coupling to an electron in a p^* orbital is proportional to the spin density on the adjacent carbon atom,

$$\langle a \rangle = Q_{\text{CHH}} r^{\text{Cp}} \quad (4.6)$$

where the parameter $Q_{\text{CHH}} = 23.0$ G, based on CH_3 , 22.5 G, based on $[\text{C}_6\text{H}_6]^-$, or 23.7 G, based on a valence-bond theoretical calculation [16]. An isotropic hyperfine coupling to H can only arise through the so-called Fermi contact interaction of the unpaired electron with the H nucleus, and this is symmetry forbidden for organic p-radicals where the H nuclei lie in the plane of symmetry. The interaction arises in a slightly more complicated way: "spin polarization". As shown in Figure 4.5, the C $2p_z$ orbital has zero probability at the H nucleus, but there is significant overlap of the C $2p_z$ and H $1s$ orbitals. Suppose the H $1s$ orbital is part of a s-bonding MO and the C $2p_z$ part of the singly-occupied p^* MO. In the overlap region of these two MO's, there is a tendency for the unpaired spin in the SOMO to polarize the pair of electrons in bonding MO such that the spins in the overlap region are parallel, necessarily leaving an oppositely oriented spin near the H nucleus.

Figure 4.5. Schematic representation of spin polarization of a C-H s-orbital by electron spin in a p^* orbital. Note that the polarization effect is far from complete; only a tiny fraction of the electron density near the H nucleus is excess spin-down.



It is sometimes assumed that there is a relation analogous to eq (4.6) for metal or ligand hyperfine couplings in spectra of organometallic radicals. Such an assumption is usually unwarranted. An isotropic hyperfine coupling has three contributions:

1. Fermi contact interaction between the nuclear spin and electron spin density in the valence-shell s-orbital
2. Fermi contact interaction between the nuclear spin and spin density in inner-shell s-orbitals arising from spin polarization by unpaired electron density in valence-shell p- or d-orbitals
3. a contribution from spin-orbit coupling.

The first contribution is positive (for a positive nuclear magnetic moment), the second is normally negative, and the third may be of either sign. Because direct involvement of hydrogen $1s$ character in the SOMO of an organic p-radical is symmetry-forbidden and spin-orbit coupling is negligible in carbon-based radicals, proton couplings in such radicals result solely from spin polarization and thus are proportional to the polarizing spin density. All three contributions are usually significant for organometallic radicals. Although there are a few cases where polarization constants, analogous to Q_{CHH} , have been estimated [17], they are of use only in a more complete analysis based on the results of a solid state ESR study.

As we will see below, g -matrices are often difficult to interpret reliably. The interpretation of isotropic g -values is even more dangerous. Thus isotropic ESR spectra should be used to characterize a radical by means of the hyperfine coupling pattern, to study its dynamical properties through linewidth effects, or to measure its concentration by integration of the spectrum and comparison with an appropriate standard, but considerable caution should be exercised in interpreting the g -value or nuclear hyperfine coupling constants.

Linewidths in Isotropic Spectra

Incomplete Averaging of Anisotropies. Isotropic ESR spectra usually show variations in linewidth from one hyperfine component to another (see, for example, Figures 4.2(a) and 4.3). The widths can often be expressed as a power series in the nuclear spin quantum numbers,

$$\text{Width} = \alpha + \sum_i \left(\beta_i m_i + \gamma_i m_i^2 + \dots \right) \quad (4.7)$$

Much of the width arises from incomplete averaging of anisotropies in the g - and hyperfine matrices (see §5), and the parameters of eq (4.7) depend on $Dg = g_{\parallel} - g_{\perp}$, $DA_i = A_{i,\parallel} - A_{i,\perp}$ and t_R , the rotational correlation time:

$$a = a_0 \mu (Dg) 2t_R \quad (4.8a)$$

$$b_i \mu Dg DA_i t_R \quad (4.8b)$$

$$g_i \mu (DA_i) 2t_R \quad (4.8c)$$

Since these terms are proportional to t_R , they increase with decreasing temperature. There are several linewidth contributions, included in a_0 , which do not depend on m_i . These include the spin-rotation interaction which increases with $1/t_R$ and thus with increasing temperature. These and other linewidth effects have been studied in some detail and are discussed elsewhere [17 - 19].

If the g - and hyperfine anisotropies are known from analysis of a solid-state spectrum, the linewidth parameters b_i and g_i can be used to compute the rotational correlation time, t_R , a useful measure of freedom of motion. Linewidths in ESR spectra of nitroxide spin labels, for example, have been used to probe the motional freedom of biological macromolecules [20]. Since t_R is related to the molecular hydrodynamic volume, V_h , and the solution viscosity, η , by :

$$t_R = \eta V_h / k_B T \quad (4.9)$$

ESR linewidths can provide a measure of the effective size of a paramagnetic molecule or ion, useful information when there is a suspicion that a radical has polymerized. Thus, for example, vanadium(IV) shows an eight-line ESR spectrum in basic aqueous solution, suggesting a monomeric unit, $[\text{VO}(\text{OH})_3(\text{H}_2\text{O})_2]^-$ [21], although previous work on the system had indicated polymers such as $\text{V}_3\text{O}_7^{2-}$ or $\text{V}_4\text{O}_9^{2-}$. Comparison of values of t_R from the basic solution linewidths with those obtained from spectra of acidic solutions containing $\text{VO}(\text{H}_2\text{O})_5^{2+}$ showed that the hydrodynamic volume of the aquo cation is actually about twice that of the basic solution species, effectively ruling out the presence of ESR-active polymers in solution [22].

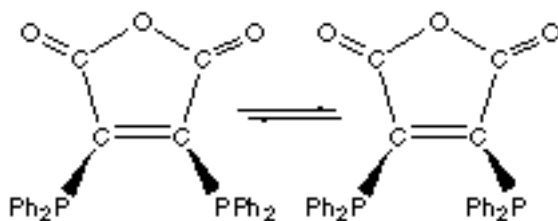
Rates of Fluxionality from Linewidths. ESR linewidths are also sensitive to processes which modulate the g -value or hyperfine coupling constants or limit the lifetime of the electron spin state. The effects are closely analogous to those observed in NMR spectra of dynamical systems. However, since ESR linewidths are typically on the order of 0.1-10 G (0.3-30 MHz), rate processes which give observable increases in linewidths must be fast. Bimolecular processes which contribute to ESR linewidths have mostly been nearly diffusion-controlled, *e.g.*, intermolecular electron exchange between naphthalene and

its anion radical [23] and reversible axial ligation of square planar copper(II) complexes [24].

The effect of rate processes on linewidths can be understood quantitatively in terms of the modified Bloch equations ([25], see also Appendix 3), or, more accurately, in terms of density matrix [26] or relaxation matrix [18, 27] formalisms. If a rate process modulates a line position through an amplitude DB (Dw in angular frequency units) by fluctuating between two states, each with lifetime t , a single line is observed with an excess width proportional to $(Dw)^2t$ when $t^{-1} \gg Dw$ – the fast exchange limit. As the lifetime increases, the line broadens to indetectability and then re-emerges as two broad lines. These shift apart and sharpen until, in the slow exchange limit ($t^{-1} \ll Dw$), two lines are observed with widths proportional to t^{-1} .

ESR spectra of the radical anion of bis-(diphenylphosphino)maleic anhydride, (3) [28], are shown in Figure 4.6. These spectra provide a good example of dynamical linewidth effects. This radical shows a 1:2:1 triplet spectrum at higher temperatures, $\langle a^P \rangle = 3.52$ G at 240 K, but the phosphorus coupling is strongly temperature dependent and extra lines appear at 200 K and below, indicating a dynamical equilibrium between two isomeric forms of the radical, one having two equivalent P nuclei (1:2:1 triplet spectrum), the other two nonequivalent P nuclei (doublet of doublets spectrum). The lines broaden with increasing temperature and coalesce at about 220 K.

These data can be understood in terms of two rotational isomers of BMA^- :



Detailed analysis led to the thermodynamic and kinetic parameters: $DH^\circ = 0.8 \pm 0.2$ kJ mol⁻¹, $DS^\circ = -4 \pm 1$ J mol⁻¹K⁻¹ ($K_{160} = 3.0$); $DH^\ddagger = 18.2 \pm 0.4$ kJ mol⁻¹, $DS^\ddagger = -30 \pm 2$ J mol⁻¹K⁻¹ ($k_{200} = 1.9 \times 10^6$).

Casagrande, *et al.* [12], used linewidth effects to study the rate of fluxionality in $(Ph_2C_2)Co(CO)[P(OMe)_3]_2$, 4. The experimental spectrum, shown in Figure 4.7(a), can be described as a

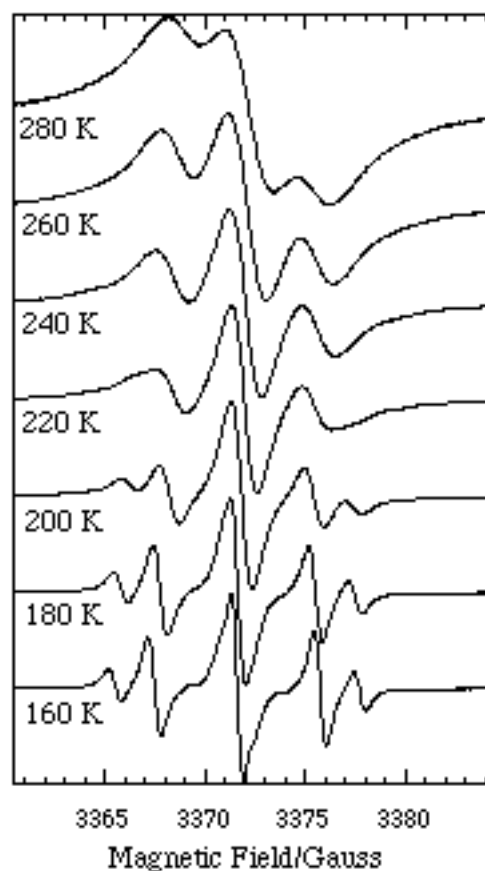


Figure 4.6. Isotropic ESR spectra of 3 in THF solution at various temperatures.

1:2:1 triplet of octets; the spectrum is complicated by a large linewidth dependence on m_{Co} , but as demonstrated in Figures 4.7(b) and 4.7(c), the central lines of the triplets are much broader than the outer lines. This radical has a distorted tetrahedral structure with the semi-occupied molecular orbital (SOMO) largely cobalt $3d_{z^2}$ in character [29]. Thus the ligand sites can be described as axial or equatorial relative to the unique z -axis. Several isomers are possible, but the ^{31}P couplings distinguish between the isomer with an axial phosphite (ax,eq) and those with either CO or the acetylene axial and both phosphites equatorial (eq,eq). The rate of interconversion between eq,eq and ax,eq isomers was estimated from the relative widths of the $m_{\text{P}} = \pm 1$ and 0 lines, given the isotropic coupling constants for the various ^{31}P nuclei (which were determined from the frozen solution spectrum [29]). The average rate was found to be approximately $2 \times 10^{10} \text{ s}^{-1}$ ($E_a = 17 \text{ kJ mol}^{-1}$) at 298 K.

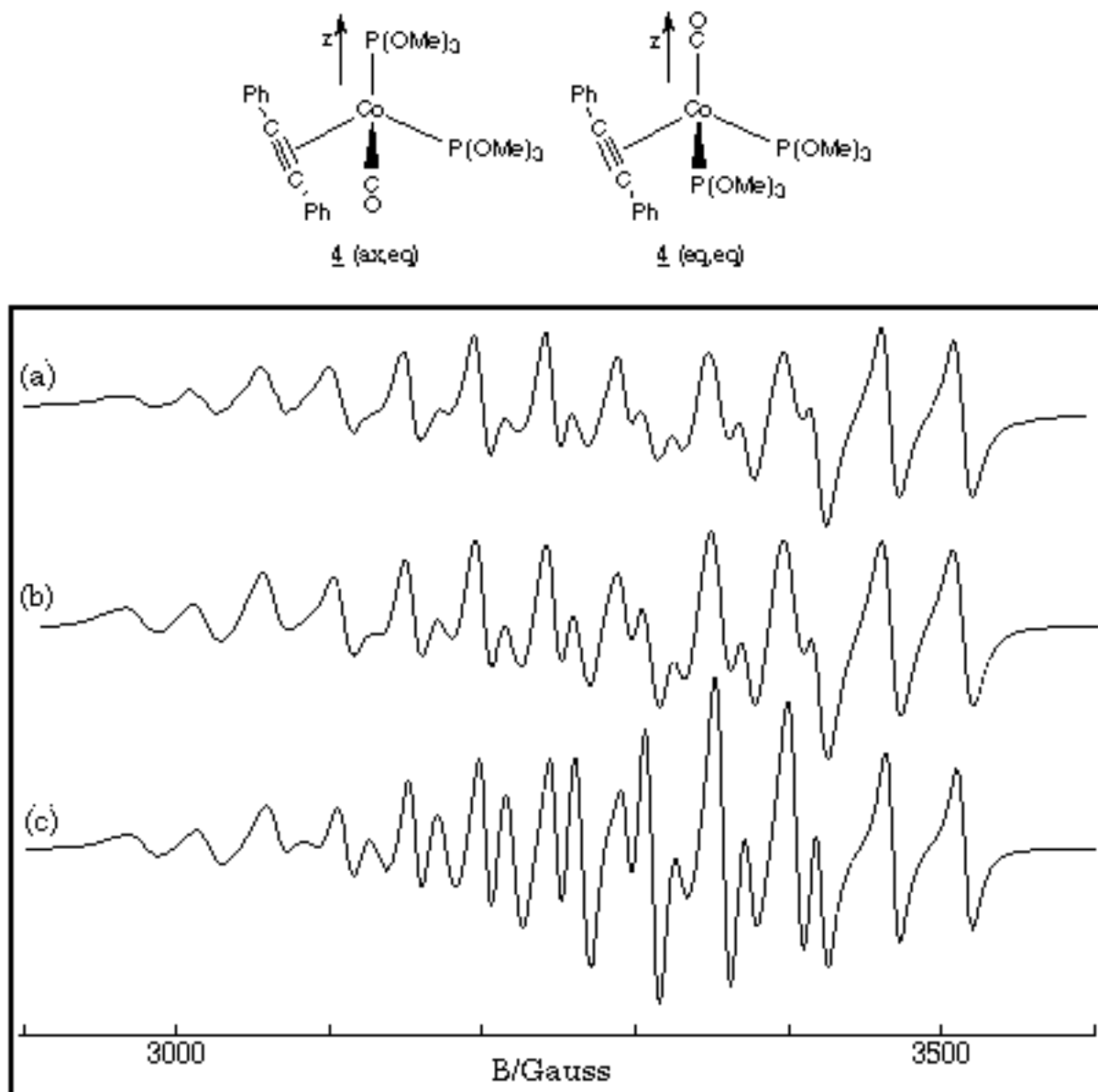


Figure 3.7. ESR spectrum of $(\text{Ph}_2\text{C}_2)\text{Co}(\text{CO})[\text{P}(\text{OMe})_3]_2$ (a) Experimental spectrum of THF solution at 290 K; (b and c) Computer-simulated spectra including (b) the m_{Co} and m_{P} linewidth dependence, and (c) the m_{Co} linewidth dependence only.

5. Anisotropic ESR Spectra

The anisotropies which lead to line broadening in isotropic ESR spectra influence solid-state spectra more directly. Accordingly a more complex spin Hamiltonian is required to interpret such spectra

$$\hat{H}_s = \mu_B \vec{B} \cdot \vec{g} \cdot \vec{S} + \sum_i \vec{I}_i A_i \cdot \vec{S} \quad (5.1)$$

In eq (5.1), g and A_i are 3×3 matrices representing the anisotropic Zeeman and nuclear hyperfine interactions. In general, a coordinate system can be found (the g -matrix principal axes) in which g is diagonal. If g and A_i are diagonal in the same coordinate system, we say that their principal axes are coincident.

In species with two or more unpaired electrons, a fine structure term must be added to the spin Hamiltonian to represent electron spin-spin interactions. We will confine our attention here to radicals with one unpaired electron ($S = 1/2$) but will address the $S > 1/2$ problem in Section 6.

Nuclear quadrupole interactions introduce line shifts and forbidden transitions in spectra of radicals with nuclei having $I > 1/2$. In practice, quadrupolar effects are observable only in very well-resolved spectra or in spectra of radicals with nuclei having small magnetic moments and large quadrupole moments. The most extreme case of a small magnetic moment to quadrupole moment ratio is that of $^{191}\text{Ir}/^{193}\text{Ir}$, and spectra of $[\text{Ir}(\text{CN})_6]^{3-}$ [30], $[\text{Ir}(\text{CN})_5\text{Cl}]^{4-}$ and $[\text{Ir}(\text{CN})_4\text{Cl}_2]^{4-}$ [31], and

$[\text{Ir}_2(\text{CO})_2(\text{PPh}_3)_2(\text{m-RNNR})_2]^+$, $\text{R} = \text{p-tolyl}$ [32], show easily recognizable quadrupolar effects. Other nuclei for which quadrupolar effects might be expected include $^{151}\text{Eu}/^{153}\text{Eu}$, $^{155}\text{Gd}/^{157}\text{Gd}$, ^{175}Lu , ^{181}Ta , ^{189}Os , and ^{197}Au . When quadrupolar effects are important, it is usually necessary to take account of the nuclear Zeeman interaction as well. The nuclear quadrupole and nuclear Zeeman interactions add two more terms to the spin Hamiltonian. Since these terms considerably complicate an already complex situation, we will confine our attention here to nuclei for which quadrupolar effects can be neglected.

When a radical is oriented such that the magnetic field direction is located by the polar and azimuthal angles, q and f , relative to the g -matrix principal axes, the resonant field is given, to first order in perturbation theory, by [33]

$$B = B_0 - \sum_i \frac{A_i m_i}{g \mu_B} \quad (5.2) \quad \text{where } B_0 = \frac{h \nu}{g \mu_B} \quad (5.3)$$

$$g^2 = g_x^2 \sin^2 q \cos^2 f + g_y^2 \sin^2 q \sin^2 f + g_z^2 \cos^2 q \quad (5.4)$$

$$A_i^2 = A_{iz}^2 S_{ix}^2 + A_{iy}^2 S_{iy}^2 + A_{iz}^2 S_{iz}^2 \quad (5.5)$$

$$S_{ik} = [g_x \sin q \cos f l_{ixk} + g_y \sin q \sin f l_{iyk} + g_z \cos q l_{izk}] / g \quad (5.6)$$

and the l_{ijk} are direction cosines indicating the orientation of the k th principal axis of the i th hyperfine matrix relative to the j th g -matrix principal axis. When the matrix principal axes are coincident, only one of the l_{ijk} of eq (4.6) will be nonzero. When the hyperfine matrix components are large, second-order terms [33] must be added to eq (5.2); these result in down-field shifts, proportional to m_i^2 .

Solid-State ESR Spectra

So long as they are dilute (to avoid line broadening from intermolecular spin exchange), radicals can be studied in the solid state as solutes in single crystals, powders, glasses or frozen solutions. Radicals can be produced *in situ* by UV- or g-irradiation of a suitable precursor in a crystalline or glassy matrix. While many organometallic radicals have been studied in this way [34], it is often easier to obtain solid state ESR spectra by freezing the liquid solution in which the radical is formed. A variety of techniques then can be used to generate radicals, *e.g.*, chemical reactions, electrochemical reduction or oxidation, or photochemical methods. Furthermore, the radical is studied under conditions more closely approximating those in which its reaction chemistry is known.

Spectra of Dilute Single Crystals. Spectra of radicals in a dilute single crystal are obtained for a variety of orientations, usually with the field perpendicular to one of the crystal axes. Spectra usually can be analyzed as if they were isotropic to obtain an effective *g*-value and hyperfine coupling constants. Since the *g*- and hyperfine matrix principal axes are not necessarily the same as the crystal axes, the matrices, written in the crystal axis system usually will have off-diagonal elements. Thus, for example, if spectra are obtained for a variety of orientations in the crystal *xy*-plane, the effective *g*-value is

$$g^2 = (g_{xx} \cos f + g_{yx} \sin f)^2 + (g_{xy} \cos f + g_{yy} \sin f)^2 + (g_{xz} \cos f + g_{yz} \sin f)^2 \quad (5.7)$$

$$\text{or } g^2 = K_1 + K_2 \cos 2f + K_3 \sin 2f \quad (5.8)$$

$$\text{where } K_1 = (g_{xx}^2 + g_{yy}^2 + g_{xz}^2 + g_{yz}^2 + 2g_{xy}^2)/2 \quad (5.9a)$$

$$K_2 = (g_{xx}^2 - g_{yy}^2 + g_{xz}^2 - g_{yz}^2)/2 \quad (5.9b)$$

$$K_3 = g_{xy}(g_{xx} + g_{yy}) + g_{xz}g_{yz} \quad (5.9c)$$

A sinusoidal plot of g^2 vs f can be analyzed to determine K_1 , K_2 , and K_3 . Exploration of another crystal plane gives another set of K 's which depend on other combinations of the g_{ij} ; eventually enough data are obtained to determine the six independent g_{ij} (\mathbf{g} is a symmetric matrix so that $g_{ij} = g_{ji}$). The \mathbf{g}^2 -matrix then is diagonalized to obtain the principal values and the transformation matrix, elements of which are the direction cosines of the \mathbf{g} -matrix principal axes relative to the crystal axes. An analogous treatment of the effective hyperfine coupling constants leads to the principal values of the \mathbf{A}^2 -matrix and the orientation of its principal axes in the crystal coordinate system.

Analysis of Powder Spectra. Since ESR spectra are normally recorded as the first derivative of absorption vs. field, observable features in the spectrum of a powder correspond to molecular orientations for which the derivative is large in magnitude or changes in sign. For any spin Hamiltonian, there will be minimum and maximum resonant fields at which the absorption changes rapidly from zero, leading to a large value of the derivative and features which resemble positive-going and negative-going absorption lines. Peaks in the absorption envelope correspond to derivative sign changes and lead to features resembling isotropic derivative lines. The interpretation of a powder spectrum thus depends on the connection of the positions of these features to the \mathbf{g} - and hyperfine matrix components.

Early treatments of powder patterns attempted to deal with the spatial distribution of resonant fields by analytical mathematics [35]. This approach led to some valuable insights but the algebra is much too complex when nonaxial hyperfine matrices are involved. Consider the simplest case: a single resonance line without hyperfine structure. The resonant field is given by eq (5.3). Features in the first derivative spectrum correspond to discontinuities or turning points in the absorption spectrum which arise when $\partial B/\partial q$ or $\partial B/\partial f$ are zero,

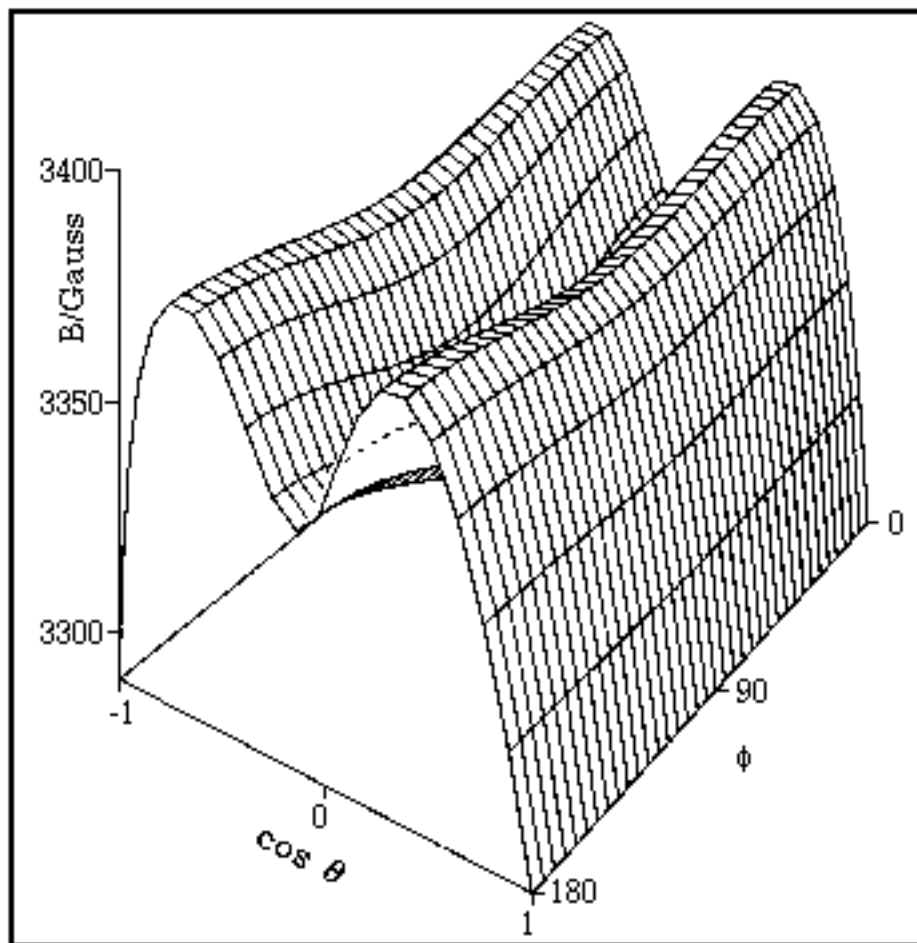
$$\frac{\partial B}{\partial \theta} = \frac{h\nu}{\mu_B} \frac{g_z^2 - g_1^2}{g^3} \sin \theta \cos \theta = 0 \quad (5.10a)$$

$$\text{or } \frac{\partial B}{\partial \phi} = \frac{h\nu}{\mu_B} \frac{g_x^2 - g_y^2}{g^3} \sin^2 \theta \sin \phi \cos \phi = 0 \quad (5.10b)$$

These equations have three solutions: (i) $q = 0$; (ii) $q = 90^\circ$, $f = 0$; and (iii) $q = f = 90^\circ$. Since q and f are in the g -matrix axis system, observable features are expected for those fields corresponding to orientations along the principal axes of the g -matrix. This being the case, the principal values of the g -matrix are obtained from a straightforward application of eq (5.3).

Powder spectra with hyperfine structure often can be interpreted similarly with spectral features identified with orientation of the magnetic field along one of the g - and hyperfine matrix principal axes. However, this simple situation often breaks down. Using a first-order theory and one hyperfine coupling, Ovchinnikov and Konstantinov [36] have shown that eqs (5.10) may have up to six solutions corresponding to observable spectral features. Three of these correspond to orientation of B along principal axes, but the "extra lines" correspond to less obvious orientations. Even more extra lines may creep in when the spin Hamiltonian is treated to second order or when there is more than one hyperfine coupling. The problem is illustrated by the resonant field *vs.* $\cos q$ and f surface shown in Figure 5.1, corresponding to the $m_{Cu} = -3/2$ "line" in the spectrum of $\text{Cu}(\text{acac})_2$ ($g = 2.0527, 2.0570, 2.2514$; $A_{Cu} = 27.0, 19.5, 193.4 \times 10^{-4} \text{ cm}^{-1}$) [36]. The minimum resonant field, $B = 3290.7 \text{ G}$, corresponds to B along the z -axis ($\cos q = \pm 1$). With B along the x -axis ($\cos q = 0$, $f = 0^\circ$), the surface shows a saddle point at 3344.3 G , and with B along the y -axis ($\cos q = 0$, $f = 90^\circ$), there is a local minimum at 3325.5 G . In addition, another saddle point occurs in the yz -plane at $B = 3371.2 \text{ G}$ ($\cos q = \pm 0.482$, $f = 90^\circ$); the only maximum is in the xz -plane at $B = 3379.0 \text{ G}$ ($\cos q = \pm 0.459$, $f = 0^\circ$). Thus five features are expected and indeed are shown in the computer-simulated spectrum of $\text{Cu}(\text{acac})_2$ shown in Figure 5.2. The two high-field features correspond to off-axis field orientations and thus are "extra lines". The situation is more complex when the g - and hyperfine matrix principal axes are noncoincident (see below); in this case, none of the features need correspond to orientation of B along a principal axis direction.

Figure 5.1.
Res-onant field as
a function of cos
 q and f for the
 $m_{Cu} = -3/2$ "line"
of the frozen
solution spectrum
of $\text{Cu}(\text{acac})_2$; ESR
parameters from
reference 36.



Since the analytical approach is so complicated, powder patterns have usually been analyzed by comparing the experimental spectrum with a spectrum, computer-simulated using estimates of the g - and hyperfine matrix components. Parameters are then adjusted and another simulation computed until the fit is satisfactory (or the experimentalist loses patience with the problem). The most straightforward computer simulation method [37] involves computation of the resonant magnetic field using eq (5.2) for *ca.* 105 values of $\cos \theta$ and ϕ for each set of nuclear spin quantum numbers. The field is then divided into equal increments and the number of times the resonant field falls between B_i and B_{i+1} is plotted *vs.* B to give an approximation to the unbroadened absorption spectrum. The absorption spectrum is then broadened by numerical convolution with a line shape function and differentiated to give the desired simulation. Although the "cut and try" approach to spectrum analysis works reasonably well when there are small numbers of parameters, analysis of a complex spectrum is exceedingly tedious.

DeGray and Rieger [38] have developed a computer algorithm to locate powder pattern features in spectra, given estimates of the spin Hamiltonian parameters. The method employs a search of the resonant field surface in $\cos \theta, \phi$ space for maxima, minima, and saddle points. Since the search procedure requires computation of B for ~ 100 orientation, the method is much faster than a complete

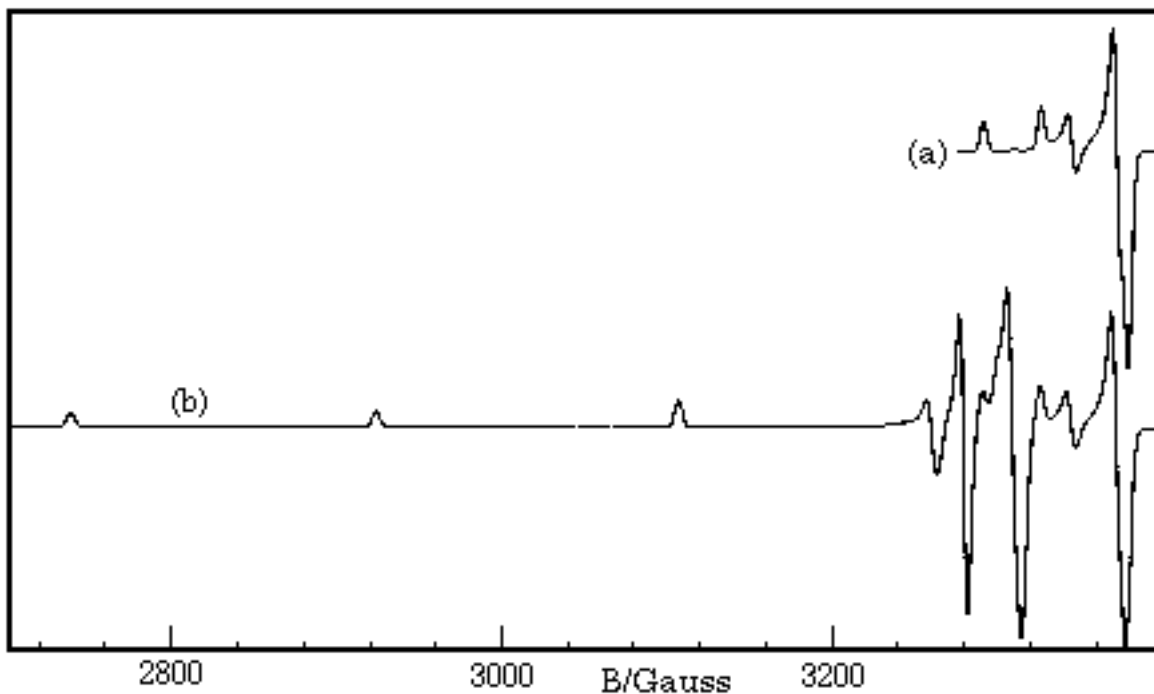


Figure 5.2. Computer-simulated first-derivative ESR powder spectrum of Cu(acac)₂. (a) Features corresponding to $m_{Cu} = -3/2$; (b) Complete spectrum.

simulation. The predicted locations of spectral features then are compared with the experimental values and the parameters refined using a nonlinear least-squares method. Using this method, relatively complex powder patterns can be analyzed, provided that the spectrum is sufficiently well resolved that enough features can be located and identified to determine the parameters. Even with least-squares fitting, however, comparison of the experimental spectrum with a computer simulation is required to check the assignments of spectral features.

Interpretation of the g -Matrix

The g -value of a free electron is a scalar, $g_e = 2.00232$. In a radical species, g becomes a matrix because of the admixture of orbital angular momentum into S through spin-orbit coupling. The components of the g -matrix thus differ from g_e to the extent that p-, d- or f-orbital character has been incorporated and differ from one another, depending on which p-, d- or f-orbitals are involved.

In general, the components of the g -matrix are given by

$$g_{ij} = g_e \delta_{ij} + 2 \sum_k \sum_{m \neq 0} \frac{\langle m | \mathbf{L}_{ki} | 0 \rangle \langle 0 | \mathbf{L}_{kj} | m \rangle}{E_0 - E_m} \quad (5.11)$$

where the indices i and j refer to molecular coordinate axes (x, y, z), k sums over atoms with unpaired electron density, and m sums over filled and empty molecular orbitals with energy E_m (E_0 is the energy of the SOMO); z_k is the spin-orbit coupling constant for atom k , and \mathbf{L}_{ki} is the i -component orbital angular momentum operator for atom k . The integrals $\langle m | \mathbf{L}_{ki} | 0 \rangle$ are easily computed if the MO's are written as linear combination of real p or d atomic orbitals. The results of operation by \mathbf{L}_i on these functions is shown in Table 5.1. Thus, for example, $\langle z^2 | \mathbf{L}_x | y \rangle = i$ and $\langle z^2 | \mathbf{L}_y | xz \rangle = -\sqrt{3} i$.

Notice that dz^2 is unique among the d-orbitals in that \mathbf{L}_z does not couple it to any other orbital. Thus if

the major metal contribution to the SOMO is dz_2 , g_z will be close to the free electron value. Accordingly, when one g -matrix component is found close to the free electron value, it is often taken as evidence for a dz_2 -based SOMO; such reasoning should be applied with caution, however, since cancellation of negative and positive terms in eq (5.11) could have the same effect.

Spin-orbit coupling to empty MO's ($E_0 - E_m < 0$) gives a negative contribution to g_{ij} whereas coupling to filled MO's has the opposite effect. Thus ESR spectra of $d1$ vanadium(IV) complexes generally have g -values less than g_e (admixture of empty MO's) whereas $d9$ copper(II) complexes have g -values greater than g_e (admixture of filled MO's).

Since the g -matrix has only three principal values and there are almost always many potentially interacting molecular orbitals, there is rarely sufficient information to interpret a g -matrix with complete confidence. When a well resolved and reliably assigned optical spectrum is available, the energy differences, $E_0 - E_m$, are known and can be used in eq (5.11). Extended Hückel MO calculations can be useful (but don't trust EHMO energies!), but one is most commonly reduced to arguments designed to show that the observed g -matrix is consistent with the interpretation placed on the hyperfine matrix.

Table 5.1. Angular momentum operations on the real p and d orbitals.

	l_x	l_y	l_z
$ x\rangle$	0	$-i z\rangle$	$i y\rangle$
$ y\rangle$	$i z\rangle$	0	$-i x\rangle$
$ z\rangle$	$-i y\rangle$	$i x\rangle$	0
$ x^2-y^2\rangle$	$-i yz\rangle$	$-i xz\rangle$	$2i xy\rangle$
$ xy\rangle$	$i xz\rangle$	$-i yz\rangle$	$-2i x^2-y^2\rangle$
$ yz\rangle$	$i x^2-y^2\rangle + \sqrt{3}i z^2\rangle$	$i xy\rangle$	$-i xz\rangle$
$ xz\rangle$	$-i xy\rangle$	$i x^2-y^2\rangle - \sqrt{3}i z^2\rangle$	$i yz\rangle$
$ z^2\rangle$	$-\sqrt{3}i yz\rangle$	$\sqrt{3}i xz\rangle$	0

Interpretation of the Hyperfine Matrix

Electron-nuclear hyperfine coupling arises mainly through two mechanisms:

1. The Fermi contact interaction between the nuclear spin and s-electron spin density; this contribution is isotropic and has been discussed above.
2. The electron spin-nuclear spin magnetic dipolar interaction; this contribution is almost entirely anisotropic, *i.e.*, neglecting spin-orbit coupling, the average dipolar contribution to the hyperfine coupling is zero.

The general form of the dipolar contribution to the hyperfine term of the Hamiltonian is

$$\hat{H}_{\text{dipolar}} = g_e g_N \mu_B \mu_N \left\langle \Psi_{\text{SOMO}} \left| \frac{\vec{S} \vec{I}}{r^3} - \frac{3(\vec{S} \cdot \vec{r})(\vec{I} \cdot \vec{r})}{r^5} \right| \Psi_{\text{SOMO}} \right\rangle \quad (5.12)$$

where g_e and g_N are the electron and nuclear g -values, μ_B and μ_N are the Bohr and nuclear magnetons, and the matrix element is evaluated by integration over the spatial coordinates, leaving the spins as operators. Equation (5.12) can then be written

$$\hat{H}_{\text{dipolar}} = \vec{I} \cdot \mathbf{A}_d \cdot \vec{S} \quad (5.13)$$

where \mathbf{A}_d is the dipolar contribution to the hyperfine matrix,

$$\mathbf{A} = A_0 \mathbf{E} + \mathbf{A}_d \quad (5.14)$$

(\mathbf{E} is the unit matrix). In evaluating the matrix element of eq (5.12), the integration over the angular variables is quite straightforward. The integral over r , however, requires a good atomic orbital wavefunction. Ordinarily, the integral is combined with the constants as a parameter

$$P = g_e g_N \mu_B \mu_N \left\langle r^{-3} \right\rangle \quad (5.15)$$

P has been computed using Hartree-Fock atomic orbital wavefunctions and can be found in several published tabulations [39-42]. Because of the $\langle r^{-3} \rangle$ dependence of P , dipolar coupling of a nuclear spin with electron spin density on another atom is usually negligible.

If an atom contributes p_x , p_y , and p_z atomic orbitals to the SOMO

$$c_x |x\rangle + c_y |y\rangle + c_z |z\rangle \quad (5.16)$$

the total p-orbital spin density is (in the Hückel approximation, i.e., neglecting overlap):

$$\rho_p = c_x^2 + c_y^2 + c_z^2 \quad (5.17)$$

and the dipolar contribution to the hyperfine matrix can be written

$$(\mathbf{A}_d)_{ij} = (2/5) P l_{ij} \quad (5.18)$$

where the l_{ij} are $l_{xx} = 2c_x^2 - c_y^2 - c_z^2$ (5.19a)

$$l_{yy} = -c_x^2 + 2c_y^2 - c_z^2 \quad (5.19b)$$

$$l_{zz} = -c_x^2 - c_y^2 + 2c_z^2 \quad (5.19c)$$

$$l_{ij} = -3c_i c_j \quad (i - j) \quad (5.19d)$$

The dipolar hyperfine matrix for p-orbitals can always be written

$$\mathbf{A}_d = (2/5)P \rho^p \begin{pmatrix} 2 & 0 & 0 \\ 0 & -1 & 0 \\ 0 & 0 & -1 \end{pmatrix} \quad (5.20)$$

The p-orbital axis corresponds to the positive principal value of the matrix. When the p-orbitals are written as hybrids, the orbital shape is unchanged, but the principal axes of the hyperfine matrix, which reflect the spatial orientation of the hybrid p-orbital, differ from those in which the SOMO was formulated. Thus, for example, a p-hybrid with $cx = cz$ ($cy = 0$) corresponds to a p-orbital with the major axis in the xz -plane and halfway between the x - and z -axes (Euler angle $b = 45^\circ$).

Similarly, if an atom contributes d atomic orbitals to the SOMO,

$$c_z^2 |z^2\rangle + c_{yz} |yz^2\rangle + c_{xz} |xz^2\rangle + c_{x^2-y^2} |x^2-y^2\rangle + c_{xy} |xy\rangle \quad (5.21)$$

the total d-orbital spin density is (in the Hückel approximation):

$$\rho^d = (c_z^2)^2 + (c_{yz}^2)^2 + (c_{xz}^2)^2 + (c_{x^2-y^2}^2)^2 + (c_{xy}^2)^2 \quad (5.22)$$

and the dipolar contribution to the hyperfine matrix is [43]

$$(\mathbf{A}d)_{ij} = (2/7)P l_{ij} \quad (5.23)$$

where P is given by eq (5.15) and the l_{ij} are:

$$l_{xx} = -(c_z^2)^2 - 2(c_{yz}^2)^2 + (c_{xz}^2)^2 + (c_{x^2-y^2}^2)^2 + (c_{xy}^2)^2 - 2\sqrt{3}(c_z^2)(c_{x^2-y^2}) \quad (5.24a)$$

$$l_{yy} = -(c_z^2)^2 + (c_{yz}^2)^2 - 2(c_{xz}^2)^2 + (c_{x^2-y^2}^2)^2 + (c_{xy}^2)^2 + 2\sqrt{3}(c_z^2)(c_{x^2-y^2}) \quad (5.24b)$$

$$l_{zz} = 2(c_z^2)^2 + (c_{yz}^2)^2 + (c_{xz}^2)^2 - 2(c_{x^2-y^2}^2)^2 - 2(c_{xy}^2)^2 \quad (5.24c)$$

$$l_{xy} = -2\sqrt{3}(c_z^2)(c_{xy}) + 3(c_{yz})(c_{xz}) \quad (5.24d)$$

$$l_{yz} = \sqrt{3}(c_z^2)(c_{yz}) + 3(c_{xz})(c_{xy}) - 3(c_{yz})(c_{x^2-y^2}) \quad (5.24e)$$

$$l_{xz} = \sqrt{3}(c_z^2)(c_{xz}) + 3(c_{yz})(c_{xy}) + 3(c_{xz})(c_{x^2-y^2}) \quad (5.24f)$$

The dipolar contribution to the hyperfine matrix for a pure d-orbital is

$$\mathbf{A}_d = (\pm 2/7)P \rho^d \begin{pmatrix} 2 & 0 & 0 \\ 0 & -1 & 0 \\ 0 & 0 & -1 \end{pmatrix} \quad (5.25)$$

where the positive sign applies for dz^2 and the lower sign to the other four orbitals. Hybrid combinations of dyz , dxz , and dxy or dx^2-y^2 and dxy give a d-orbital of the same shape and the same dipolar matrix,

though the principal axes in general are different from the axes in which the SOMO was formulated. Other hybrid orbitals are generally of different shape, reflected by different principal values of the dipolar matrix, usually with different principal axes.

Spin-orbit coupling perturbs these results, adding terms to the diagonal matrix components on the order of $P(g_i - g_e)$. These can be neglected only when the g -matrix anisotropy is small. Calculation of the spin-orbit coupling corrections is fairly straightforward for mononuclear complexes where the SOMO is composed mainly of d -orbitals from a single metal [6,44,45]. In radicals with two or more transition metals, the spin-orbit coupling calculation is seriously nontrivial. A major part of the problem is that the solution must be gauge-invariant, that is, it must not depend on the choice of coordinate system. This problem was addressed in the context of spin-orbit coupling corrections to the g -matrix [46], with eq (5.11) as the result, but it has received only cursory examination with regard to spin-orbit contributions to hyperfine matrices [47]. Fortunately, polynuclear radicals containing first-row transition metals generally have g -matrix components sufficiently close to g_e that the problem can be ignored. For organometallic radicals with second- and third-row transition metals, the problem is urgent; it is to be hoped that some theoretician will deem the problem worthy of attention.

The AO composition of the SOMO can often be deduced from the dipolar hyperfine matrix, particularly when the radical has enough symmetry to restrict possible hybridization. Thus an axial hyperfine matrix can usually be interpreted in terms of coupling to a single p - or d -orbital. A departure from axial symmetry may be due to spin-orbit coupling effects, if (for example) $A_{||} = A_z$ and $A_x - A_y \propto P(g_x - g_y)$. If the departure from axial symmetry is larger, it is usually caused by d -orbital hybridization. The procedure is best illustrated by example.

Example—A low-spin Manganese(II) Complex

The spectrum of the low-spin manganese(II) complex, $[\text{Mn}(\text{dppe})_2(\text{CO})(\text{CNBu})]^{2+}$, **5** (dppe = $\text{Ph}_2\text{PCH}_2\text{CH}_2\text{PPh}_2$) [48], in a $\text{CH}_2\text{Cl}_2/\text{THF}$ glass is shown in Figure 5.3a. The spin Hamiltonian parameters, obtained from a least-squares fit of the field positions of the spectral features [49], are given in Table 2, and a computer simulation based on those parameters is shown in Figure 5.3b.

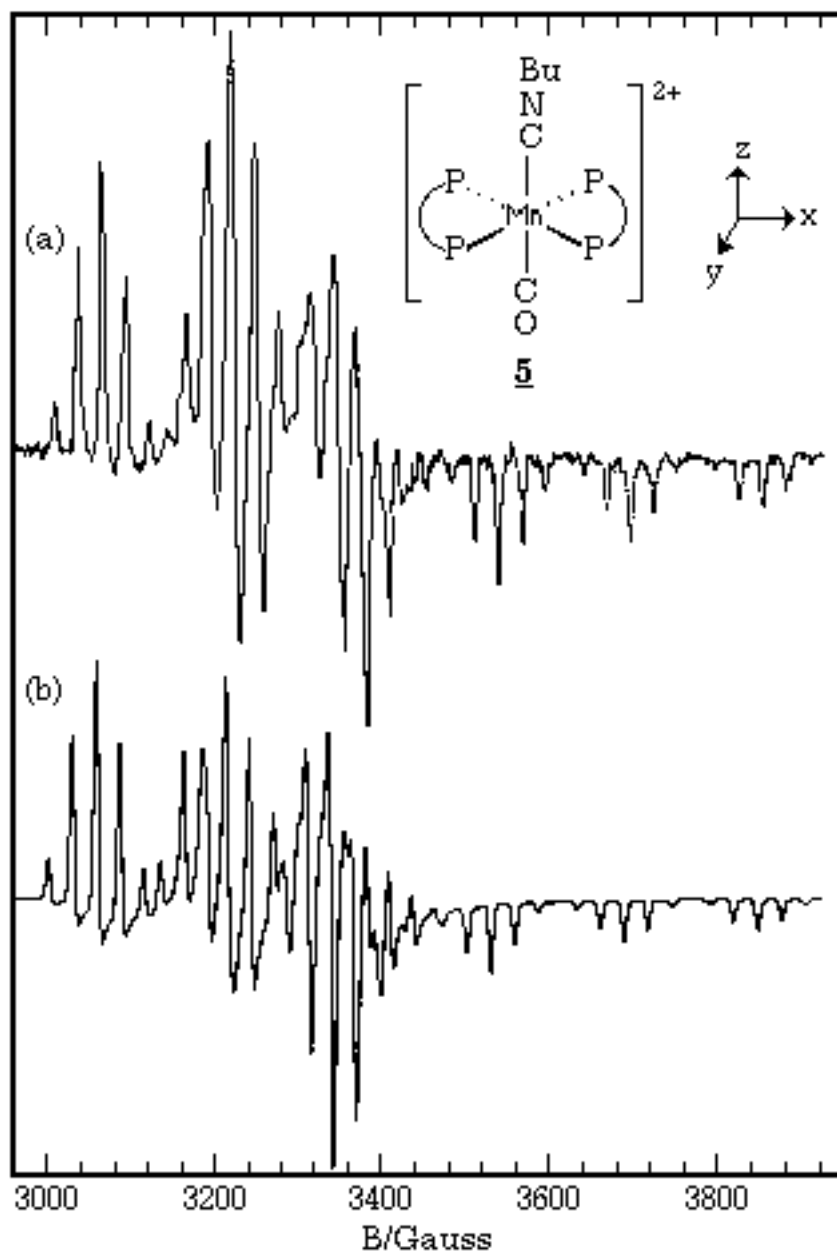
Table 2. ESR Parameters for $[\text{Mn}(\text{dppe})_2(\text{CO})(\text{CNBu})]^{2+}$.

g	$A_{\text{Mn}}/10^{-4} \text{ cm}^{-1}$	$A_{\text{P}}/10^{-4} \text{ cm}^{-1}$
2.107	30.2	27.2
2.051	20.6	25.3
1.998	146.9	26.4

5 has approximate C_{2v} symmetry, although the actual symmetry is reduced to C_2 or C_s , depending on the conformation of the ethylene bridges of the dppe ligands. Since **5** has a nominal d^5 configuration, the SOMO is expected to be one of the " t_{2g} " orbitals of an idealized octahedral complex— dxz (**b1**), dyz (**b2**), or dx^2-y^2 (**a1**), where the representations refer to C_{2v} . The energies of the dxz and dyz orbitals are expected to be lowered by back-donation into the 1^* orbitals of the CO and CNBu ligands so that the

SOMO is most likely based on dx^2-y^2 , possibly with some symmetry-allowed dz^2 admixture,

Figure 5.3. (a) ESR spectrum of **5** in a $\text{CH}_2\text{Cl}_2/\text{THF}$ glass (49); (b) Computer simulation using the parameters of Table 2.



$$|\text{SOMO}\rangle = a|z^2\rangle + b|x^2-y^2\rangle + \dots \quad (5.26)$$

Although the isotropic spectrum of **5** was not sufficiently resolved to unambiguously determine $\langle A^{\text{Mn}} \rangle$, other closely related species give isotropic couplings on the order of 60-70 G [49]; if we assume an isotropic coupling in this range, all three matrix components must have the same sign. If the isotropic hyperfine coupling is negative, as expected if it arises mostly through polarization of inner-shell s orbitals, we have $\langle A^{\text{Mn}} \rangle = -65.9 \times 10^{-4} \text{ cm}^{-1}$. Assuming that the SOMO is mostly dx^2-y^2 , ($b \gg a$) and including the appropriate spin-orbit coupling corrections, we have [29,45]

$$A_z - \langle A \rangle = P \left[\frac{4}{7} (a^2 - b^2) - \frac{2}{3} \Delta g_z - \frac{5}{42} (\Delta g_x + \Delta g_y) \right] \quad (5.27)$$

With $Dgz = -0.004$, $(Dgx + Dgy) = 0.154$, and $P = 207.6 \times 10^{-4} \text{ cm}^{-1}$ [40], we get $(a^2 - b^2) = -0.655$.

The departure from axial symmetry is due to spin-orbit coupling and/or dx^2-y^2/dz^2 hybridization,

$$A_x - A_y = P \left[-\frac{8\sqrt{3}}{7} ab + \frac{17}{14} (\Delta g_x - \Delta g_y) \right] \quad (5.28)$$

Substituting the parameters, we have $ab = \pm 0.058$. (The upper sign applies if the components are listed in the order x, y, z in Table 2, the lower sign if the order is y, x, z) Finally, we get $b^2 = 0.660$, $a^2 = 0.005$. The dz^2 component is not really significant, given the accuracy of the data and the theory, *i.e.*, most of the departure from axial symmetry can be explained by the spin-orbit coupling correction.

Using eq (5.11), the g -matrix components are found to be

$$\Delta g_{xx} = 2\sum_{\text{Mn}} \sum_{\mathbf{k}} \frac{b^2 c_{yz\mathbf{k}}^2}{E_0 - E_{\mathbf{k}}} \quad (5.29a)$$

$$\Delta g_{yy} = 2\sum_{\text{Mn}} \sum_{\mathbf{k}} \frac{b^2 c_{xz\mathbf{k}}^2}{E_0 - E_{\mathbf{k}}} \quad (5.29b)$$

$$\Delta g_{zz} = 2\sum_{\text{Mn}} \sum_{\mathbf{k}} \frac{4b^2 c_{xy\mathbf{k}}^2}{E_0 - E_{\mathbf{k}}} \quad (5.29c)$$

If we assume coupling with single pure dyz , dxz , and dxy orbitals, we have $DE_{yz} = 16z$, $DE_{xz} = 19z$, $DE_{xy} = -110z$, qualitatively consistent with the expected MO energy level scheme.

Example: Some Cobalt(0) Radical Anions

ESR spectra of $[\text{CpCo}(1,3\text{-COD})]^-$, **6**, in frozen THF solution and $[\text{CpCo}(1,5\text{-COD})]^-$, **7**, in frozen DMF were reported by Geiger and coworkers [50] and are reproduced in Figures 5.4a and 5.5a. These spectra have been reinterpreted to give the parameters shown in Table 3; computer-simulated spectra based on these parameters are shown in Figures 5.4b and 5.5b. Also shown in the table are the ESR parameters for $[(\text{C}_5\text{Ph}_5)\text{Co}(\text{CO})_2]^-$, **8** [44].

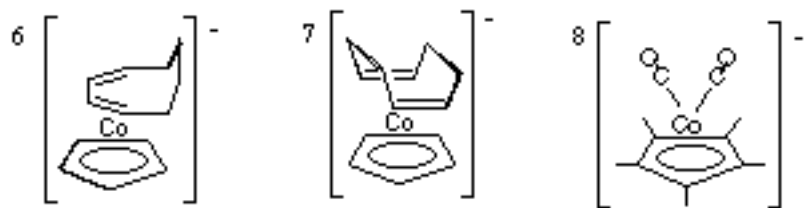


Table 3. ESR parameters for Cobalt(0) Radical Anions.

Radical Anion	g_x	g_y	g_z	A_{xa}	A_{ya}	A_{za}
$[\text{CpCo}(1,5\text{-COD})]^-$	2.171	2.027	1.985	(-)158.6	(-)36.7	(-)45.8
$[\text{CpCo}(1,3\text{-COD})]^-$	2.151	2.027	1.997	(-)139.2	(-)36.4	(-)38.2
$[(\text{C}_5\text{Ph}_5)\text{Co}(\text{CO})_2]^-$	2.018	2.041	1.995	(-)157.9	(-)16.8	(-)44.1

a Units of 10^{-4} cm^{-1} . b From reference 44.

The hyperfine matrix components must have identical signs in order that the average values match the observed isotropic couplings; we assume the signs are negative since the isotropic couplings almost certainly arise from polarization of inner shell s orbitals (see below).

The SOMO in these radicals is expected from extended Hückel MO calculations [50,51] to be primarily cobalt $3d_{yz}$ in character. In the C_s symmetry of the radicals, dyz belongs to the a'' representation and d -hybridization is possible only with d_{xy} . Assuming that such hybridization is negligible, the g -matrix components are given by [44]

$$\Delta g_{xx} = 2\tau_{Co} \sum_k \frac{\alpha^2 (c_{x^2-y^2k})^2 + 3\alpha^2 (c_{z^2k})^2}{E_0 - E_k} \quad (5.30a)$$

$$\Delta g_{yy} = 2\tau_{Co} \sum_k \frac{\alpha^2 (c_{xyk})^2}{E_0 - E_k} \quad (5.30b)$$

$$\Delta g_{zz} = 2\tau_{Co} \sum_k \frac{\alpha^2 (c_{xz k})^2}{E_0 - E_k} \quad (5.30c)$$

The dipolar contribution to the hyperfine matrix is given by eq (5.20), but spin-orbit coupling contributions are significant. These often can be ex-

pressed in terms of the g -matrix components (as in the $Mn(II)$ example discussed above), but here spin-orbit coupling with the four other d -orbitals contributes somewhat differently to the g -matrix and to the hyperfine matrix. The simplest way of expressing the hyperfine matrix is in terms of the isotropic coupling, the x -component, and the departure from axial symmetry,

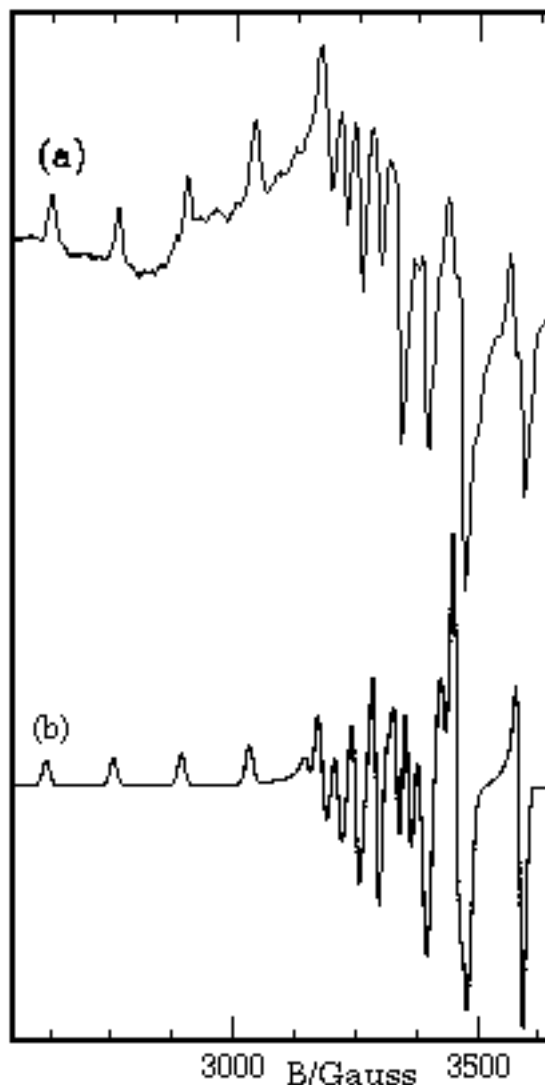


Figure 5.4. ESR spectrum of $[CpCo(1,3-COD)]^-$; (a) experimental spectrum in frozen THF solution (from reference 50); (b) computer-simulation, based on the parameters of Table 3.

$$\langle A \rangle = A_s + \frac{1}{3} P (\Delta g_{xx} + \Delta g_{yy} + \Delta g_{zz}) \quad (5.31a)$$

$$A_x - \langle A \rangle = P \left[-\frac{4}{7} a^2 + \frac{2}{3} \Delta g_{xx} - \frac{5}{42} (\Delta g_{yy} + \Delta g_{zz}) \right] \quad (5.31b)$$

$$A_y - A_z = \frac{17}{14} P (\Delta g_{yy} + \Delta g_{zz}) + \frac{6a^2 P}{7} \left(\frac{1}{\Delta E_{x^2-y^2}} - \frac{1}{\Delta E_{z^2}} \right) \quad (5.31c)$$

With the assumed signs of the hyperfine components of Table 3, eq (5.31b) can be used unambiguously to compute $a^2 = rd$ with the results shown in Table 4.

Since $3dyz/4s$ admixture is symmetry-forbidden for these radicals, the Fermi contact contribution to the isotropic coupling must be entirely from spin polarization,

$$A_s = Qd \quad (5.32)$$

Thus we can obtain an independent estimate of the d-electron spin density from the values of A_s , taking $Qd = -131 \text{ } \forall \text{ } 10^{-4} \text{ cm}^{-1}$, estimated from the isotropic cobalt coupling in $[\text{PhCCo}_3(\text{CO})_9]^-$. The results are shown in the last column of Table 4. The spin densities estimated from the isotropic couplings are consistently about 10% higher than those from the dipolar coupling matrix, suggesting a systematic error in one of the parameters, but a reliable ordering of the spin densities.

Table 4. d-Electron spin densities in cobalt(0) radical anions.

Radical Anion	rd	Asa	As/Qd
$[\text{CpCo}(1,5\text{-COD})]^-$	0.681	-97.0	0.740
$[\text{CpCo}(1,3\text{-COD})]^-$	0.591	-87.2	0.666
$[(\text{C}_5\text{Ph}_5)\text{Co}(\text{CO})_2]^-$ -b	0.540	-77.4	0.591

a in units of 10^{-4} cm^{-1} .

The g -matrix presents an interesting problem in these cases. EHMO calculations [50,51] suggest that the SOMO is the highest-energy MO which is primarily cobalt 3d in character. At lower energy is an orbital with dxz character and still lower, but grouped at about the same energy, are MO's with dx^2-y^2 , dxy , and dz^2 contributions. Equations (5.30) then would suggest that $Dg_{xx}/4 \text{ } \forall \text{ } Dg_{yy} < Dg_{zz}$. With the assignments of Table 4, the first relationship is approximately correct for **6** and **7**, but very poor for **8**. The second relationship is not found for any of the anions. Reversing the y and z assignments makes the agreement worse. In discussing this problem for **8** [44], we postulated admixture of some cobalt 4p character in the SOMO,

$$|\text{SOMO}\rangle = a|yz\rangle + b|y\rangle + \dots \quad (5.33)$$

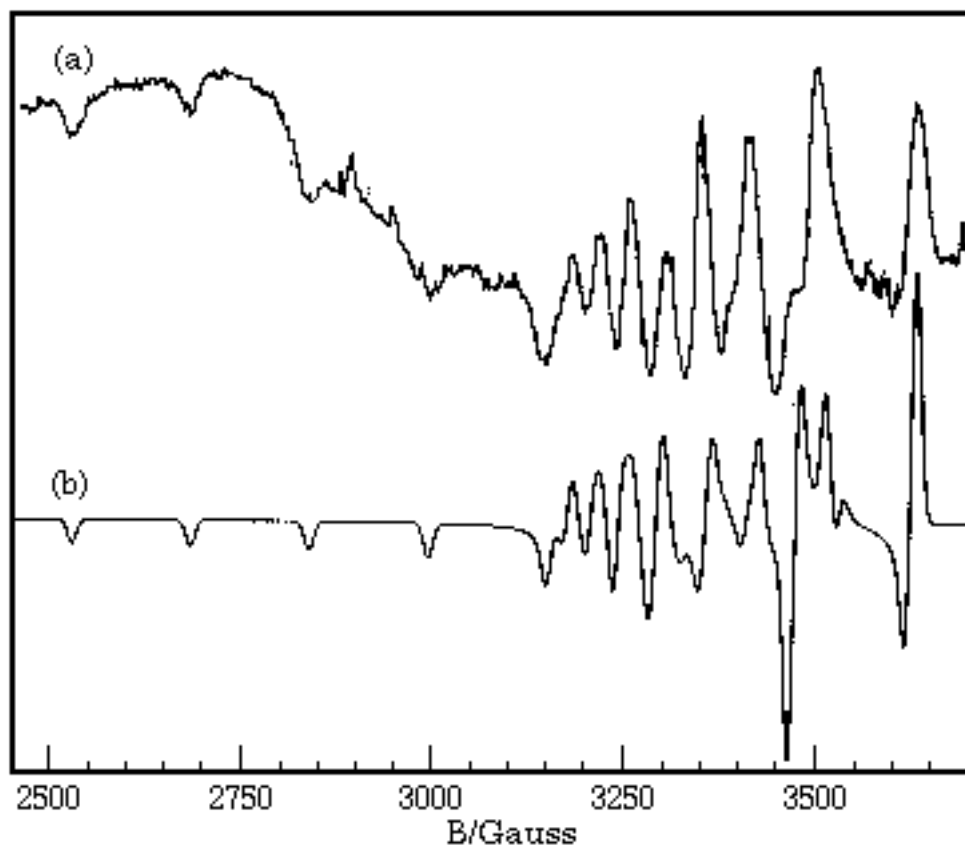


Figure 5.5. ESR spectrum of [CpCo(1,5-COD)]⁻; (a) experimental spectrum in frozen DMF solution (from reference 50); (b) computer-simulation, based on the parameters of Table 3

which would result in additional contributions to g_{xx} and g_{zz} ,

$$g_{xx}(p) = 2zp^2/DE_z \text{ and } g_{zz}(p) = 2zp^2/DE_x \quad (5.34)$$

where zp is the cobalt 4p spin-orbit coupling parameter ($zp \text{ \AA} \text{ } zd/3$). If MO's with significant p_z or p_x character lie just above the SOMO, then g_{xx} and g_{zz} would be less positive than expected from eqs (5.30), possibly even negative. g_{xx} is indeed smaller than expected for **8** and EHMO calculations do indeed suggest a MO with significant p_z character just above the SOMO in energy; this orbital is apparently substantially higher in energy in **6** and **7**. A MO with significant p_x character, at about the same energy for all three anions, is implied by these results but is unsubstantiated by the reported EHMO calculations.

Noncoincident Matrix Axes

In general, the g - and nuclear hyperfine coupling matrices, \mathbf{g} and \mathbf{A}_i , can be written in diagonal form with three principal values— g_x , g_y , g_z and A_{ix} , A_{iy} , A_{iz} . In textbooks on ESR [2-7], it is usually assumed that the same set of principal axes diagonalizes all the relevant matrices. While this is sometimes true, there are many instances where the principal axes are noncoincident [52].

Symmetry Considerations. Kneubühl [53,54] has given a detailed group theoretical analysis of symmetry restrictions on the orientations of g - and hyperfine matrix principal axes. His results are summarized in Table 5. For a nucleus sharing all the molecular symmetry elements (*e.g.*, the metal

nucleus in a mononuclear complex), the hyperfine matrix is subject to the same restrictions as the g -matrix. In orthorhombic or axial symmetry, such nuclear hyperfine matrices necessarily share principal axes with the g -matrix. In monoclinic symmetry, one hyperfine axis is also a g -matrix axis, but the other two may be different. In triclinic symmetry (C_1 or C_i), none of the three principal axes need be shared by the g -matrix and hyperfine matrix. The hyperfine matrix for a ligand atom (or for a metal in polynuclear complexes) is constrained only by the symmetry elements which the nucleus shares with the molecule.

Table 5. Symmetry restrictions on g -matrix components.

Symmetry	Point Groups	Restrictions on Diagonal Elements	Restrictions on Off-Diagonal Elements	Required Matrix Axes
Triclinic	C_1, C_i	none	none	none
Monoclinic	C_2, C_s, C_{2h}	none	$g_{xz} = g_{yz} = 0$	z
Orthorhombic	C_{2v}, D_2, D_{2h}	none	$g_{xz} = g_{yz} = g_{xy} = 0$	x, y, z
Axial	$C_n, C_{nv}, C_{nh}, D_n, D_{nd}, D_{nh}, n > 2$	$g_{xx} = g_{yy}$	$g_{xz} = g_{yz} = g_{xy} = 0$	x, y, z

Although symmetry considerations often permit g - and hyperfine matrix principal axes to be noncoincident, there are relatively few cases of such noncoincidence reported in the literature. Most of the examples discussed by Pilbrow and Lowrey in their 1980 review [52] are cases of transition metal ions doped into a host lattice at sites of low symmetry. This is not to say that matrix axis noncoincidence is rare but that the effects have only rarely been recognized.

Experimental Determination of Matrix Axis Orientations. We have seen that spectra of dilute single crystals are analyzed in a way that gives the orientations of the g - and hyperfine matrix principal axes relative to the crystal axes. Historically, most of the information on noncoincident matrix axes is derived from such studies.

At first glance, it would appear that all orientation dependence should be lost in the spectrum of a randomly oriented sample and that location of the g - and hyperfine matrix principal axes would be impossible. While it is true that there is no way of obtaining matrix axes relative to molecular axes from a powder pattern, it is frequently possible to find the orientation of a set of matrix axes relative to those of another matrix.

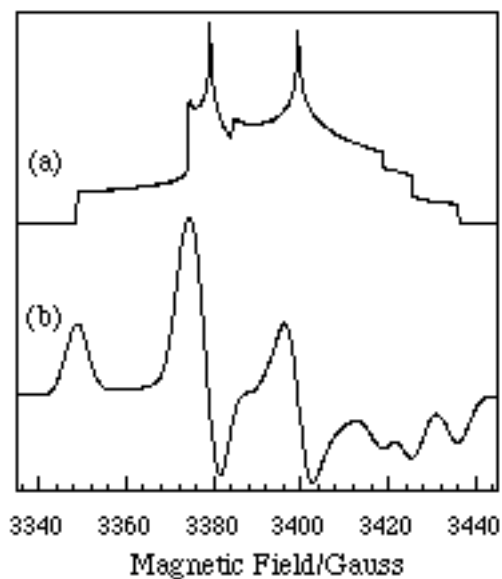
The observable effects of matrix axis noncoincidence on powder patterns range from blatantly obvious to negligible. In general, the effects of axis noncoincidence will be more noticeable if two (or more) matrices have large anisotropies which are comparable in magnitude, *e.g.*, $D_{gm}BB \text{ \AA} DA$. *This follows from the fact that minimum and maximum resonant fields are determined by a competition between*

extrema in the angle-dependent values of g and A . Consider the case of noncoincident g - and hyperfine matrix axes. For large values of $|m_I|$, the field extrema will be determined largely by the extrema in the effective hyperfine coupling and will occur at angles close to the hyperfine matrix axes, but for small $|m_I|$, the extrema will be determined by extrema in the effective g -value and will correspond to angles close to the g -matrix axes. The result of such a competition is that a series of features which would be equally spaced (to first order) acquires markedly uneven spacings.

There are two corollaries stemming from this generalization. Since spin 1/2 nuclei give only two hyperfine lines, there can be no variation in spacings. Thus powder spectra cannot be analyzed to extract the orientations of hyperfine matrix axes for such important nuclei as ^1H , ^{13}C , ^{19}F , ^{31}P , ^{57}Fe , and ^{103}Rh . Secondly, since the observable effects in powder spectra depend on the magnitude of the matrix anisotropies, the principal axes of the hyperfine matrix for a nucleus with small hyperfine coupling generally cannot be located from a powder spectrum, even though the relative anisotropy may be large.

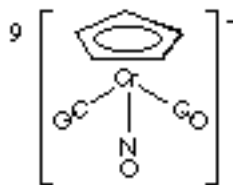
Example—Chromium Nitrosyl Complex

A good example of the effect of g - and hyperfine matrix axis noncoincidence is the ESR spectrum of $[\text{CpCr}(\text{CO})_2\text{NO}]^-$, **9**, studied by Geiger and coworkers [55] and



and shown in Figure 5.6. The g - and ^{14}N hyperfine matrices are approximately axial for this radical, but the g_{\parallel} axis lies close to the perpendicular plane of the hyperfine matrix. If the g_{\parallel} axis was exactly in the A^{\wedge} plane, the three negative-going $g_{\parallel} A^{\wedge}$ features, corresponding to resonant field maxima, would be evenly spaced. In fact, the spacings are very uneven, far more so than can be explained by second-order shifts. The effect can be understood, and the spectrum simulated virtually exactly, by assuming that the g_{\parallel} axis is about 15° out of the A^{\wedge} plane.

Figure 5.6. Computer-simulated (a)absorption and (b) first-derivative spectra of **9**.



Example—Iron Pentacarbonyl Ions

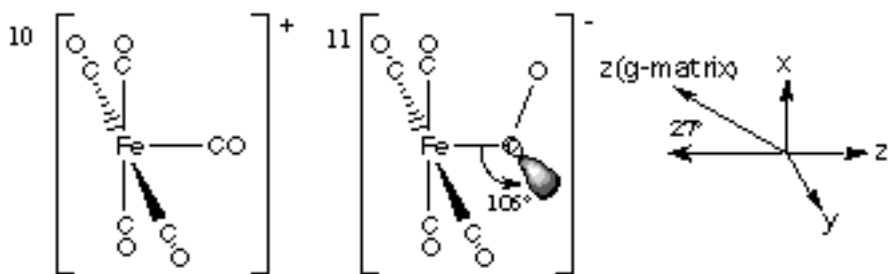
Two particularly interesting organometallic examples were reported by Morton, Preston and coworkers [56,57]. Spectra of single crystals of $\text{Cr}(\text{CO})_6$, doped with ^{13}C - or ^{57}Fe -enriched $\text{Fe}(\text{CO})_5$ and g -irradiated at 77 K, showed two different radicals. One species, identified as $\text{Fe}(\text{CO})_5^+$, showed coupling to ^{57}Fe and to a unique ^{13}C nucleus with axial hyperfine matrices sharing principal axes with the g -matrix [56]. Coupling was also observed to four other ^{13}C nuclei with identical coupling matrices but with the major axis approximately along the g -matrix x -axis for two nuclei and along the g -matrix

y-axis for the other two. The parameters are listed in Table 6. If the radical is square pyramidal (C_{4v}) $Fe(CO)_5^+$, **10**, the principal axes of the g -matrix must be the molecular axes (the C_4 axis and normals to the reflection planes). The iron atom and the carbon of the axial CO group have the full symmetry of the group and so these hyperfine matrices must share principal axes with the g -matrix. The four equatorial carbonyl carbons, on the other hand, lie in reflection planes, but not on the C_4 -axis and so are symmetry-required to share only one principal axis with the g -matrix. In fact, the major matrix axes for the equatorial carbons are tilted slightly in the $-z$ direction from the ideal locations along the $\pm x$ and $\pm y$ axes. The g -matrix suggests that the metal contribution is dz^2 and the iron hyperfine matrix then can be used to estimate about 55% iron 3d and 34% axial carbon 2p $_z$ spin density. The spin density on the equatorial carbons then is mostly negative and due to spin polarization.

Table 6. ESR Parameters for $Fe(CO)_5^+$ and $Fe(CO)_5^-$.^a

$Fe(CO)_5^+$:	$g_{ } = 2.001$	$A_{ Fe} = (+)9.4$	$A_{ C1} = (+)19.6$	$A_{ C2-C5} = (+)6.4$
	$g^{\wedge} = 2.081$	$A^{\wedge}Fe = (-)6.2$	$A^{\wedge}C1 = (-)17.6$	$A^{\wedge}C2-C5 = (+)8.6$
$Fe(CO)_5^-$:	$g_1 = 1.989$	$A_1Fe = (+)6.7$	$A_1C1 = (+)87.4$	
	$g_2 = 2.003$	$A_2Fe = (-)4.5$	$A_2C1 = (+)70.7$	
	$g_3 = 2.010$	$A_3Fe = (-)3.2$	$A_3C1 = (+)65.7$	

^a Coupling constants in units of 10^{-4} cm^{-1} . Data from references 56 and 57.



The other species observed in irradiated $Fe(CO)_5$ -doped crystals of $Cr(CO)_6$ also showed coupling to ^{57}Fe , to a unique ^{13}C , and to four other carbons. However, in this case g , A_{Fe} , and A_{C1} have only one matrix axis in common (that corresponding to the third component of each matrix listed in Table 6). The other ^{57}Fe hyperfine axes are rotated by about 27° and those of the ^{13}C hyperfine matrix by about 48° relative to the g -matrix axes. Insufficient data were accumulated to determine the complete hyperfine matrices for the other four carbons, but the components are considerably smaller ($4 - 15 \times 10^{-4} \text{ cm}^{-1}$). The hyperfine matrices suggest about 38% iron 3d z^2 , 18% carbon 2p, and 6% carbon 2s spin densities. Using detailed arguments regarding the orientation of the g -matrix axes relative to the crystal axes, the

authors conclude that the carbon 2p axis is oriented at about 106° relative to the Fe-C bond axis and that the Fe-C-O bond angle is about 119° .

The most striking feature of these results is the orientation of the unique ^{13}C hyperfine matrix axes, relative to those of the ^{57}Fe hyperfine axes. This orientation led Fairhurst, *et al.*[57], to assign the spectrum to $\text{Fe}(\text{CO})_5^-$, **11**, and to describe the species as a substituted acyl radical. However, these authors did not discuss the orientation of the g -matrix axes. The y -axis, normal to the reflection plane, is common to all three matrices. The x - and z - axes of the g -matrix, on the other hand are oriented about 27° away from the corresponding ^{57}Fe hyperfine matrix axes. Since the iron d-orbital contribution to the SOMO appears to be nearly pure d_{z^2} , the ^{57}Fe hyperfine matrix major axis must correspond to the local z -axis, assumed to be essentially the Fe-C bond. Thus we must ask: Why are the g -matrix axes different? The SOMO can be written

$$|\text{SOMO}\rangle = a|z^2, \text{Fe}\rangle + b_x|x, \text{C}\rangle + b_z|z, \text{C}\rangle \quad (5.35)$$

where $a = 0.62$, $b_x = -0.41$, and $b_z = 0.12$. Spin-orbit coupling will mix the SOMO with MO's having iron dyz or dxz character, but dyz is involved in the p orbitals of the C=O group,

$$|y\rangle = c_{yz}|yz, \text{Fe}\rangle + c_y|y, \text{C}\rangle \quad (5.36)$$

Assuming that there is only one p orbital close enough in energy to couple significantly, eq (5.11) gives the g -matrix components:

$$\Delta g_{xx} = 2\zeta_{\text{Fe}} \frac{3a^2 c_{yz}^2 + \sqrt{3} ab_z c_y c_y}{\Delta E_\pi} \quad (5.37a)$$

$$\Delta g_{yy} = 2\zeta_{\text{Fe}} \frac{3a^2 c_{xz}^2}{\Delta E_{xz}} \quad (5.37b)$$

$$Dg_{zz} = 0 \quad (5.37c)$$

$$g_{xz} = -2\zeta_{\text{Fe}} \frac{\sqrt{3} ab_x c_y c_y}{\Delta E_\pi} \quad (5.37d)$$

The g -matrix can be diagonalized by rotation about the y -axis by the angle b ,

$$\tan 2\beta = \frac{2g_{xz}}{g_{xx} - g_{zz}} = \frac{-2\sqrt{3} ab_x}{3a^2(c_{yz}/c_y) + \sqrt{3} ab_z} \quad (5.38)$$

With $b = 27^\circ$, this expression gives $c_{yz}/c_y \hat{A} 0.5$, a reasonable result.

This may be a rather general effect; if the unpaired electron in a radical is delocalized asymmetrically, and other MO's are similarly delocalized, the g -matrix will have off-diagonal elements which may be large enough to shift the principal axes away from the molecular coordinate system.

Example—Another low-spin Manganese(II) Complex

The low-spin manganese(II) complex, $[\text{Mn}(\text{dppe})_2(\text{CO})(\text{CNBu})]^{2+}$, **5**, gave us a textbook example of a well-behaved ESR spectrum characterized by coincident g - and hyperfine matrix principal axes. The nearly identical complex, $[\text{Mn}(\text{dppm})_2(\text{CO})(\text{CN})]^+$, **12**⁺, provides us with a good example of non-coincident principal axes. The frozen solution spectrum, shown in Figure 5.7, shows that

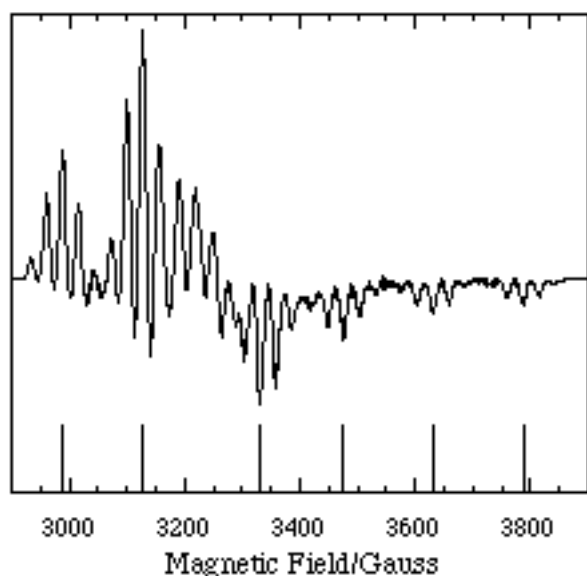


Figure 5.7. ESR spectrum of **12**⁺ in $\text{CH}_2\text{Cl}_2/\text{C}_2\text{H}_4\text{Cl}_2$ at 90 K; from reference (49).

the "parallel" features are not evenly spaced. The spectrum can be understood if the z -axes of the g - and A -matrices are displaced by $b = 19.6^\circ$. This, of course, tells us that the molecule does not have C_{2v} symmetry, and that, unlike the dppe analog, dx^2-y^2 is not the only Mn contribution to the SOMO. One way of interpreting the results is that the Mn contribution to the SOMO incorporates a small amount of dxz character. The consequence of this hybridization would be to tilt the "x" lobes of dx^2-y^2 up and down, i.e., rotation about the y -axis. The reason for this hybridization is not difficult to discover. If the CH_2 groups of the dppm ligands were coplanar with Mn, the "x" lobes of the dx^2-y^2 SOMO would be directed toward the carbon atoms and an anti-bonding

interaction would result. In order to avoid this interaction, two things happen: (1) incorporation of dxz character tilts the lobes up and down, away from the C atoms. At the same time, the x-ray structure of the Mn(II) cation shows (Figure 5.8) that the CH_2 groups tilt down and up, further decreasing the anti-bonding interaction. With only one electron in the SOMO, the anti-bonding interaction is strong enough to produce this distortion. With two electrons, the neutral parent Mn(I) complex would be expected to be even more distorted, and an x-ray structure shows that the up and down displacements of the CH_2 groups is

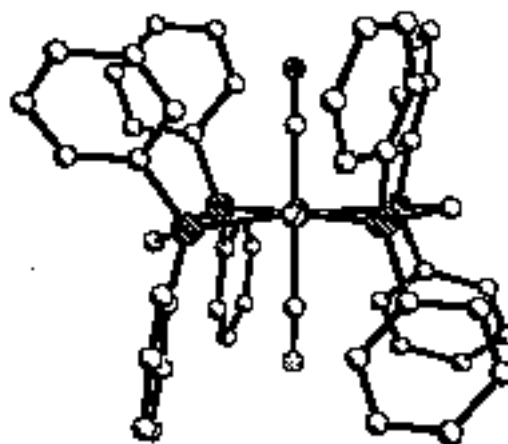


Figure 5.8. X-ray structure of **12**⁺, showing methylene groups tilted up and down to avoid anti-bonding interaction with dx^2-y^2 SOMO.

approximately doubled.

Example—Chromium(I) Piano-Stool Complex

Ordinarily, there is no way of extracting the orientation of the principal axes of the g -matrix from a powder or frozen solution ESR spectrum. However, there are exceptional circumstances in which nature is kind to the experimentalist!

Spectra of the low-spin d^5 Cr(I) complex, $[(C_5Ph_5)Cr(CO)_2PMe_3]$ **13** (58), are shown at 125 and 200 K in Figure 5.9. The low-temperature spectrum shows three sets of doublets, corresponding to the three g -components (2.104, 2.013, 1.994), each a doublet due to hyperfine coupling to ^{31}P . At 200 K, above the freezing point of toluene, the spectrum still appears as a "powder pattern", but the "perpendicular" features are nearly averaged and the "parallel" features have shifted upfield ($g_{||} = 2.090$, $g_{\perp} = 2.012$). The exceptionally bulky C_5Ph_5 ligand apparently moves very slowly at 200 K but on the ESR time scale the $Cr(CO)_2PMe_3$ moiety rotates quickly, producing a spectrum averaged about the Cr-C5 axis. With this interpretation, we can assign this axis as the principal axis for $g_{||}$ measured at 200 K and, assuming that the $g_{||}$ axis differs from the g_z axis by

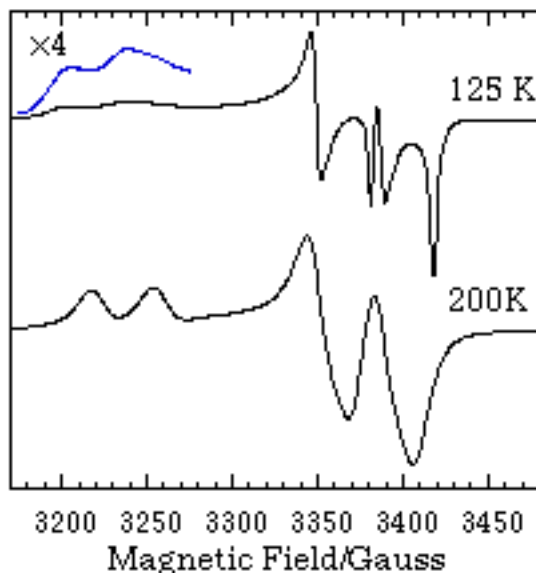


Figure 5.9. Spectra of **13** in toluene at 125 and 200 K; from reference (58).

the angle b and that g_z and g_x are averaged according to

$$2g_{||}^2 = g_z^2 + g_x^2 + (g_z^2 + g_x^2) \cos 2b$$

Substitution of the g -components gives $b = 15^\circ$

The symmetry of the complex is at most C_s , requiring one of the g -matrix principal axes to be normal to the plane of symmetry, assumed to be xz . π -back-bonding to the CO ligands is expected to lead to a hybrid SOMO. If, as suggested by extended Hückel MO calculations, the SOMO and first HOMO are of a' symmetry, and the second HOMO of a'' symmetry:

$$|\text{SOMO}\rangle = a_1 |x^2 - y^2\rangle + a_2 |z^2\rangle + a_3 |xz\rangle$$

$$|\text{HOMO}_1\rangle = b_1 |x^2 - y^2\rangle + b_2 |z^2\rangle + b_3 |xz\rangle \quad |\text{HOMO}_2\rangle = c_1 |xy\rangle + c_2 |yz\rangle$$

the g -matrix components can be computed:

$$g_{xx} = g_r + \frac{\zeta_{Co} (a_1 c_2 + \sqrt{3} a_2 c_2 + a_3 c_1)^2}{E_0 - E_2} \quad g_{yy} = g_r + \frac{\zeta_{Co} (2a_1 c_1 + a_3 c_2)^2}{E_0 - E_2}$$

$$g_{zz} = g_r + \frac{\zeta_{Co} [a_1 b_3 - a_3 b_1 + \sqrt{3} (a_3 b_2 - a_2 b_3)]^2}{E_0 - E_1}$$

$$g_{xz} = - \frac{\zeta_{Co} (2a_1 c_1 + a_3 c_2)(a_1 c_2 + \sqrt{3} a_2 c_2 + a_3 c_1)}{E_0 - E_2}$$

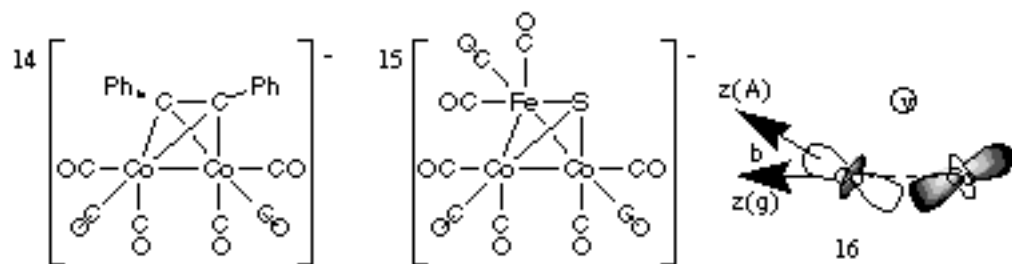
Rotation about the y -axis by β diagonalizes the matrix, and we find

$$\tan 2\beta = - \frac{2g_{xz}}{g_{yy} - g_{zz}}$$

The single experimental observable, b , is hardly enough to evaluate the LCAO coefficients for the SOMO and second HOMO, but we can compare the results of an extended Hückel MO calculation. (Since zCo and $E_0 - E_2$ cancel in the calculation of $\tan 2\beta$, the EHMO calculation could come close). The results are: $a_1 = 0.538$, $a_2 = 0.216$, $a_3 = -0.194$, $c_1 = 0.582$, $c_2 = -0.061$, $b = 14.8^\circ$. If we were to substitute these LCAO coefficients, together with the EHMO energy difference, into the expressions for g_{xx} , g_{yy} , g_{zz} , and g_{xz} , the results would be in very poor agreement with experiment; the moral here is that EHMO calculations, lacking charge self-consistency, usually have large errors in the energies, but the MO wavefunctions are often fairly accurate.

Example— $[(RCCR')Co_2(CO)_6]^-$ and $[SFeCo_2(CO)_9]^-$

Noncoincident matrix axis effects are seen in the frozen solution spectra of $[(RCCR')Co_2(CO)_6]^-$, **14** [59], and $[SFeCo_2(CO)_9]^-$, **15** [60], but the effects are rather more subtle than those discussed above.



In these cases, the g -matrix is nearly isotropic, but the principal axes of the two ^{59}Co hyperfine matrices are noncoincident. The largest hyperfine matrix component ($ay = 66.0$ G in the case of **15**) results in 15 features, evenly spaced (apart from small second-order shifts). Another series of features, less widely spaced, shows some variation in spacing and, in a few cases, resolution into components. This behavior can be understood as follows: Suppose that the hyperfine matrix y -axes are coincident and consider molecular orientations with the magnetic field in the xz -plane. To first order, the resonant field then is

$$B = B_0 - m_1 a_+ - m_2 a_- \quad (5.39)$$

where $B_0 = \hbar\nu/gmB$ and

$$a_{\pm 2} = az^2\cos^2(q \pm b) + ax^2\sin^2(q \pm b) \quad (5.40)$$

where b describes the orientation of the hyperfine matrix z -axes relative to the g -matrix z -axis. Since g is nearly isotropic, the extrema in B are determined mostly by the hyperfine term. When $m_1 = m_2$, a_+ and a_- are equally weighted and the extrema occur at $q = 0$ or 90° , but when $m_1 \neq m_2$, the extrema correspond to other angles. Consider, for example, the five components of the $m_1 + m_2 = +3$ feature. With $|az| = 53.6$ G, $|ax| = 15.5$ G, $b = 18^\circ$, the hyperfine contributions to the field extrema and the corresponding values of q are given in Table 7. In the experimental spectrum of **15**, two resolved field maximum features were seen, corresponding to the first two and the last three of the above components. Since the resolution is sensitive to the noncoincidence, it was possible to fit the experimental spectrum to obtain b quite accurately.

Table 7. Splitting of $M = 3$ features in $[\text{SFeCo}_2(\text{CO})_9]$ – Spectrum.

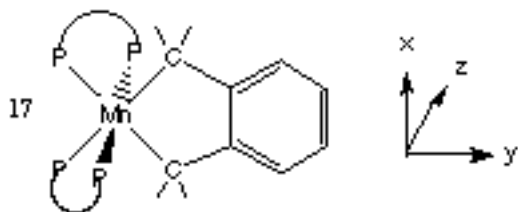
(m_1, m_2)	q_{\min}	$(B-B_0)_{\min}/\text{G}$	q_{\max}	$(B-B_0)_{\max}/\text{G}$
+7/2,-1/2	-20°	37.0	+67°	166.1
-1/2,+7/2	+20°	37.0	-67°	166.1
+5/2,+1/2	-15°	55.3	+78°	156.9
+1/2,+5/2	+15°	55.3	-78°	156.9
+3/2,+3/2	0°	66.5	90°	153.6

It is relatively easy to understand the significance of the noncoincident matrix axes in these cases. For **14**, the C_{2v} molecular symmetry permits a specific prediction of the possible matrix axis orientations. The g -matrix principal axes must be coincident with the molecular symmetry axes. The two cobalt nuclei are located in a reflection plane (which we label xz) so that symmetry requires the y -axis to be a principal axis for all three matrices. The other two axes may be rotated, relative to the molecular x - and z -axes, by $\pm b$. (Since the two nuclei are symmetrically equivalent, the rotations must be equal and opposite.)

Since the magnitudes and probable signs of the cobalt hyperfine matrices suggest a SOMO predominantly dz^2 in character, the major axes of the hyperfine matrices approximate the local z -axes at the cobalt atoms and the angular displacement indicates a bent Co-Co anti-bonding interaction, as shown in structure 16, where the C-C or Fe-S bond axis (the molecular y -axis) is perpendicular to the plane of the page. Comparison with the crystal structure of neutral $(\text{Ph}_2\text{C}_2)\text{Co}_2(\text{CO})_6$ [61] shows that these local axes are roughly in the direction of the axial carbonyl ligands (the Co-CO bond is tilted 28° away from the Co-Co vector). Thus it seems reasonable to say that the local axes on a metal are determined primarily by the more strongly interacting ligands and that bonds to other atoms can be described as bent.

Example–(o-xylene)-Mn(dmpe)₂

As part of a study of Mn(II) dialkyls, Wilkinson, Hursthouse, and coworkers [62] reported the ESR spectrum of the approximately octahedral (o-xylylene)Mn(dmpe)₂, **17**, Figure 5.10a (dmpe = Me₂PCH₂CH₂PMe₂). The spectrum was interpreted assuming coincident *g*- and hyperfine matrix axes, but a simulation based on the reported parameters gave a very poor fit to the published spectrum. On closer examination, it was realized that this is a rather



extreme example of a spectrum influenced by noncoincident *g*- and hyperfine matrix principal axes. The clue evident in the spectrum is the large gap between the $m_{\text{Mn}} = -1/2$ and $+1/2$ "parallel" features, suggesting one or more extra features. Figure 5.11 shows a set of simulated spectra for a hypothetical low-spin Mn(II) species; all seven spectra correspond to the same *g*- and hyperfine matrices, but the angle β , between the *g*- and hyperfine matrix *z*-axes, varies from 0 to 90°. As shown in Figure 5.11, it is possible to obtain spectra with more than six resolved "parallel" features. Indeed, the spectrum is sufficiently sensitive to the angle that β can be evaluated quite precisely. The final parameters for **17**, based on least-squares fitting of the positions of the resolved features and the isotropic parameters [53], are given in Table 8; a computer simulation using these parameters is shown in Figure 5.10b.

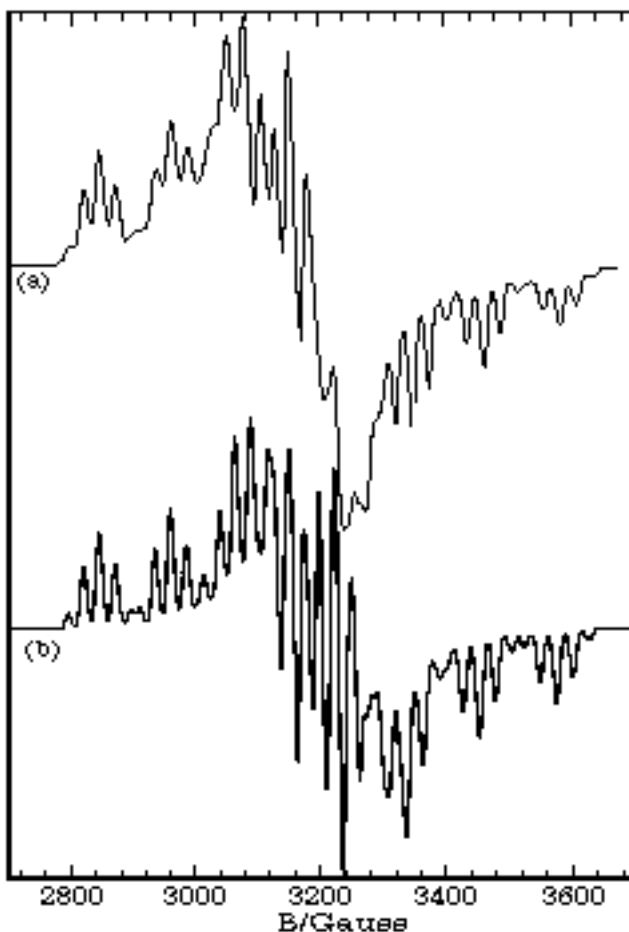


Figure 5.10. (a) ESR spectrum of (o-xylylene)Mn(dmpe)₂ in frozen toluene solution (from reference 53); (b) Computer simulation of spectrum using parameters of Table 8.

Table 8. ESR Parameters for (o-xylylene)Mn(dmpe)₂, **17.a**

<i>g</i>	<i>A</i> Mn	<i>A</i> P
2.110	27	24.5
2.035	27	24.5

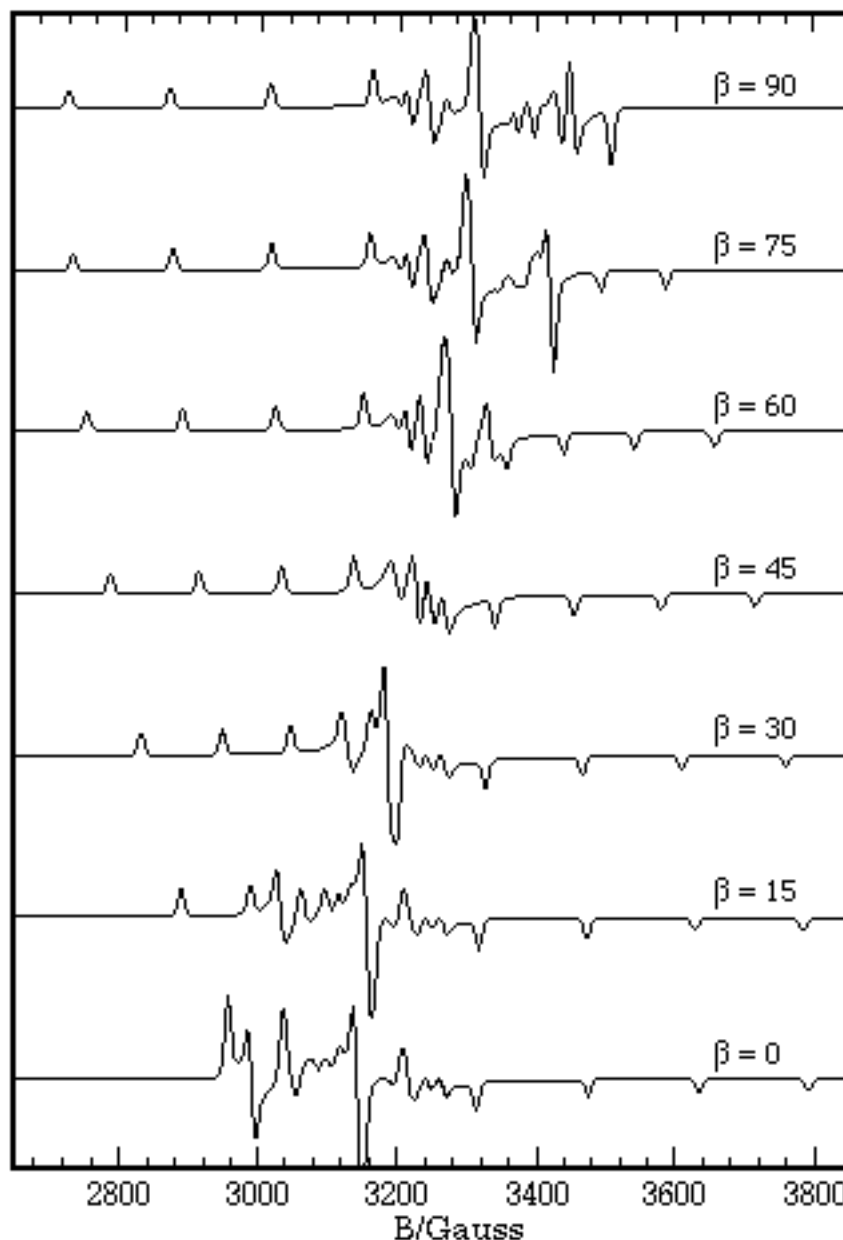
2.000

125

24.5

a Hyperfine matrix components in units of 10^{-4} cm^{-1} ; $b = 41^\circ$.

Figure 5.11.
Computer-simulated
ESR spectra for a
hypothetical low-spin
Mn(II) radical with $g =$
(2.100, 2.050, 2.000),
 $A_{\text{Mn}} = (150, 25, 25) \times$
 10^{-4} cm^{-1} , for various
 values of b , the Euler
 angle between the
 g -matrix and hyperfine
 matrix z -axes.



17 has approximate C_{2v} symmetry, but the ethylene bridges of the dmpe ligands destroy the reflection planes; the x-ray structure [53] shows a small fold at the methylene groups of the o-xylylene ligand which destroys the C_2 axis. Thus the molecule can be regarded, with increasing accuracy, as C_{2v} , C_s , C_2 , or C_1 . In order to explain the matrix axis noncoincidence, the metal contribution to the SOMO must be a d-hybrid. Since **17** is a d_5 low-spin Mn(II) species, the SOMO is expected to be dominated by one of the orbitals of the octahedral t_{2g} set— dxz , dyz , or dx^2-y^2 . This is consistent with a clue contained in the ESR parameters. The four ^{31}P couplings are apparently equivalent, and all are relatively small. Thus no lobe of the SOMO can be directed toward a phosphorus atom, and major dx_y or dz^2 contributions to the SOMO can be ruled out. Consider the twelve binary hybrids based on these orbitals which are listed

in Table 9. Since we know that the

Table 9. SOMO Candidates: Binary d-Hybrids.

Number	Representation		Major	Minor	Approx. Major	Common
	Cs	C2				
			d-AO	d-AO	HF Axis	Axis
1	a'	a	dx ² -y ²	dz ²	z	x,y,z
2	a'	-	dx ² -y ²	dyz	z	x
3	a'	-	dyz	dx ² -y ²	x	x
4	a'	-	dyz	dz ²	x	x
5	a''	-	dxz	dxy	y	x
6	-	a	dx ² -y ²	dxz	z	y
7	-	a	dxz	dx ² -y ²	y	y
8	-	a	dxz	dz ²	y	y
9	-	b	dyz	dxy	x	y
10	-	-	dx ² -y ²	dxy	z	z
11	-	-	dxz	dyz	y	z
12	-	-	dyz	dxz	x	z

hyperfine matrix major axis is not a *g*-matrix principal axis, we can immediately reject hybrids 1, 3, 4, 7, 8, and 10 for which the major axis is a common axis. Hybrids 2 and 6, 5 and 9, and 11 and 12 differ only in the *x*- and *y*-labels and are essentially indistinguishable, so that there are only three cases to consider in detail.

Hybrid 6 can be written

$$|\text{SOMO}\rangle = a|x^2-y^2\rangle + b|xz\rangle \quad (5.41)$$

Straightforward application of eqs (5.24) yields a hyperfine matrix which can be diagonalized by rotation about the *y*-axis by the angle *b*,

$$\tan 2b = -2b/a \quad (5.42)$$

The *g*-matrix can be written in relatively simple form if we assume that the only MO's close enough in energy to contribute significantly are the filled MO's, primarily dxz and dyz in character. With this

assumption, we obtain a matrix which can be diagonalized by rotation about the y -axis by b' ,

$$\tan 2\beta' = -\frac{2b/a}{1-(b/a)^2} \quad (5.43)$$

For reasonable values of the hybridization ratio, b/a up to about 0.5, b and b' can differ by only a few degrees and this kind of hybrid cannot explain the matrix axis noncoincidence. Following the same reasoning with x and y interchanged, exactly the same conclusions can be reached for hybrid 2.

Hybrids 11 and 12 are

$$|\text{SOMO}\rangle = a|xz\rangle + b|yz\rangle \quad (5.44)$$

In this case, the hyperfine matrix remains axial, independent of the hybridization ratio, although the principal axes are rotated in the xy -plane by an angle a equal to angle b of eq (5.43). Assuming that only MO's with predominantly dxz , dyz , or dx^2-y^2 character contribute, a g -matrix is found which can be diagonalized by rotation in the xy -plane by the angle a' , also given by eq (5.43). Thus this hybrid gives identical g - and hyperfine matrix principal axes for all hybridization ratios.

Finally, hybrid 9,

$$|\text{SOMO}\rangle = a|yz\rangle + b|xy\rangle \quad (5.45)$$

gives an axial hyperfine matrix with principal axes rotated in the xz -plane by an angle b , given by eq (5.43). The g -matrix is somewhat more complicated,

$$\Delta g = 2\zeta \begin{pmatrix} \frac{(ac_{x^2-y^2})^2}{\Delta E_{x^2-y^2}} + \frac{(bc_{xz})^2}{\Delta E_{xz}} & 0 & -\frac{2ab(c_{x^2-y^2})^2}{\Delta E_{x^2-y^2}} - \frac{ab(c_{xz})^2}{\Delta E_{xz}} \\ 0 & \frac{(bc_{yz})^2}{\Delta E_{yz}} & 0 \\ -\frac{2ab(c_{x^2-y^2})^2}{\Delta E_{x^2-y^2}} - \frac{ab(c_{xz})^2}{\Delta E_{xz}} & 0 & \frac{(2bc_{x^2-y^2})^2}{\Delta E_{x^2-y^2}} + \frac{(ac_{xz})^2}{\Delta E_{xz}} \end{pmatrix} \quad (5.46)$$

Diagonalization requires rotation about the y -axis by the angle b' ,

$$\tan 2\beta' = -\frac{2b}{a} \left[\frac{2Q+1}{Q-1-(b/a)^2(4Q-1)} \right] \quad (5.47)$$

where

$$Q = \frac{(c_{x^2-y^2})^2}{\Delta E_{x^2-y^2}} \bigg/ \frac{(c_{xz})^2}{\Delta E_{xz}} \quad (5.48)$$

Since the energy differences, $DE_{x^2-y^2}$ and DE_{xz} are expected to be comparable, the parameter Q is probably not far from unity. For $Q = 1$, eq (5.47) has a particularly simple form, $\tan 2b' = +2a/b$ so that, for small b/a , we expect $b \overset{\circ}{\text{A}} 0$ and $b' \overset{\circ}{\text{A}} 45^\circ$, entirely consistent with experiment. The axial hyperfine matrix is in agreement with experiment, and the principal values of the g -matrix can also be rationalized with reasonable values of Q and b/a . A small rotation of dyz about the y -axis might reflect the small displacements of the phosphorus atoms from the idealized octahedral positions.

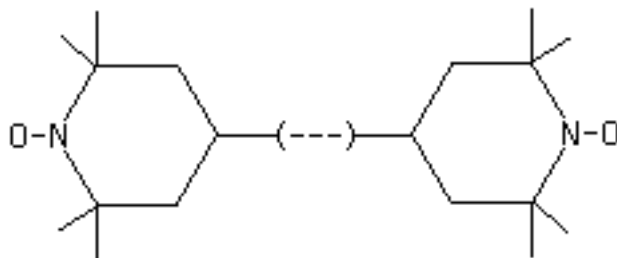
An extended Hückel MO calculation on **15** supports the assumptions made in the above analysis in that the three "t_{2g}" orbitals are indeed close together in energy and remain nearly nonbonding metal-based d-orbitals. The detailed agreement is less satisfactory: the SOMO is predicted to be primarily dx^2-y^2 with a small dxz admixture (hybrid 6 of Table 9), a result which can be ruled out from our analysis of the ESR results. The EHMO overlap matrix based on the x-ray structure suggests that the molecule is much closer to C_2 symmetry than to C_s . If we accept that conclusion, then dxz/dxy hybridization is less likely than dyz/dxy , as we tacitly assumed above.

We considered several alternative explanations for the matrix axis noncoincidence in **15**. In particular, it seemed possible that delocalization of spin density into the *o*-xylylene ligand, either through the s-bonds or into the p-system, might lead to significant contributions to the off-diagonal terms of the g -matrix. While the EHMO calculations suggest that the MO's containing dx^2-y^2 and dyz do have contributions from the carbon atoms of the *o*-xylylene group, the amount is far too small to rationalize rotation of the g -matrix axes by 41° ; indeed, to explain the effect in this way would require each of several carbon atoms to contribute 5% or more to the MO's with dx^2-y^2 or dyz character, unreasonably large considering the poor overlap of these metal d-orbitals with the relevant carbon orbitals.

6. Molecules with More than One Unpaired Electron

Molecules with two or more unpaired electrons may be divided into two classes: By far the most common examples are molecules where the unpaired electrons are contained in a set of degenerate atomic or molecular orbitals with qualitatively similar spatial distributions, e.g., an octahedral Cr(III) (**4A_{2g}**) or Ni(II) (**3A_{2g}**) complex, or a triplet state molecule like O₂, or the excited triplet states of naphthalene or benzophenone.

A second class of molecules with two unpaired electrons has the two electrons localized, to a first approximation, in different parts of the molecule. We refer to such molecules as **biradicals**. Examples are the dinitroxides, and certain binuclear vanadium(IV) and copper(II) complexes.



From the point of view of ESR spectroscopy, the distinction between molecules with one unpaired electron and those with more than one lies in the fact that electrons interact with one another; these interactions lead to additional terms in the spin Hamiltonian and additional features in the ESR spectrum. The most important electron-electron interaction is coulombic repulsion; with two unpaired electrons, repulsion leads to the singlet-triplet splitting. As we will see, this effect can be modelled by adding a

term, $J\vec{S}_1 \cdot \vec{S}_2$, to the spin Hamiltonian, where J is called the **exchange coupling constant** and turns out to be equal to the singlet-triplet splitting.

References

- 1 A. Hudson, *Electron Spin Resonance*, **1988**, *11A*, 55-76.
- 2 P. B. Ayscough, *Electron Spin Resonance in Chemistry*, Methuen, London, **1967**.
- 3 P. W. Atkins and M. C. R. Symons, *The Structure of Inorganic Radicals*, Elsevier, Amsterdam, **1967**.
- 4 A. Abragam and B. Bleaney, *Electron Paramagnetic Resonance of Transition Ions*, Clarendon Press, Oxford, **1970**.
- 5 J. E. Wertz and J. E. Bolton, *Electron Spin Resonance*, McGraw-Hill, New York, **1972**.
- 6 N. M. Atherton, *Electron Spin Resonance*, Ellis Horwood, Chichester, **1973**.
- 7 W. Gordy, *Theory and Applications of Electron Spin Resonance*, Wiley, New York, **1980**.
- 8 J. R. Pilbrow, *Transition Ion Electron Paramagnetic Resonance*, Clarendon Press, Oxford, **1990**.
- 9 F. E. Mabbs and D. Collison, *Electron Paramagnetic Resonance of d Transition Metal Compounds*, Elsevier, Amsterdam, **1992**.
- 10 G. Breit and I. I. Rabi, *Phys. Rev.* **1931**, *38*, 2082-2083.
- 11 S. I. Weissman, J. Townsend, G. E. Paul, and G. E. Pake, *J. Chem. Phys.* **1953**, *21*, 2227.
- 12 L. V. Casagrande, T. Chen, P. H. Rieger, B. H. Robinson, J. Simpson, and S. J. Visco, *Inorg. Chem.* **1985**, *23*, 2019-2025.
- 13 B. M. Peake, P. H. Rieger, B. H. Robinson, and J. Simpson, *Inorg. Chem.* **1979**, *18*, 1000-1005.
- 14 A. R. Boate, J. R. Morton, and K. F. Preston, *J. Mag. Reson.* **1976**, *24*, 259-268.
- 15 R. W. Fessenden and R. H. Schuler, *J. Chem. Phys.* **1963**, *39*, 2147.
- 16 M. Karplus and G. K. Fraenkel, *J. Chem. Phys.* **1961**, *35*, 1312.
- 17 R. Wilson and D. Kivelson, *J. Chem. Phys.* **1966**, *44*, 154; P. W. Atkins and D. Kivelson, *J. Chem. Phys.* **1966**, *44*, 169.
- 18 G. K. Fraenkel, *J. Phys. Chem.* **1967**, *71*, 139-171.
- 19 W. B. Lewis and L. O. Morgan, in R. L. Carlin (Ed.), *Transition Met. Chem., Vol. 4*, Marcel Dekker, New York, **1968**, pp. 33-112.
- 20 B. H. Robinson and A. H. Beth, *Electron Spin Resonance* **1983**, *8*, 346-377.
- 21 M. M. Iannuzzi and P. H. Rieger, *Inorg. Chem.* **1975**, *14*, 2895-2899.
- 22 M. M. Iannuzzi, C. P. Kubiak, and P. H. Rieger, *J. Phys. Chem.* **1976**, *80*, 541-545.
- 23 R. L. Ward and S. I. Weissman, *J. Am. Chem. Soc.* **1957**, *79*, 2086-2090.
- 24 B. J. Corden and P. H. Rieger, *Inorg. Chem.* **1971**, *10*, 263-272.

- 25** H. S. Gutowsky, D. W. McCall, and C. P. Slichter, *J. Chem. Phys.* **1953**, *21*, 279-292. See also reference 6, pp 309-313.
- 26** J. I. Kaplan, *J. Chem. Phys.* **1958**, *28*, 278-282; **1958**, *29*, 462; S. Alexander, *ibid.* **1962**, *37*, 967-974, 974-980. See also reference 6, pp 313-323.
- 27** See also reference 6, pp 323-327.
- 28** N. W. Duffy, R. R. Nelson, M. G. Richmond, A. L. Rieger, P. H. Rieger, B. H. Robinson, D. R. Tyler, J. C. Wang and K. Yang, *Inorg. Chem.* **1998**, *37*, 4849.
- 29** J. A. DeGray, Q. Meng, and P. H. Rieger, *J. Chem. Soc. Faraday I* **1987**, *83*, 3565-3573.
- 30** N. V. Vugman, A. O. Caride, and J. Danon, *J. Chem. Phys.* **1973**, *59*, 4418-4422.
- 31** N. V. Vugman and N. M. Pinhal, *Mol. Phys.* **1983**, *49*, 1315-1319.
- <32/b>** J. A. DeGray, P. H. Rieger, N. G. Connelly and G. Garcia, *J. Magn. Reson.*, **1990**, , 376.
- 33** P. H. Rieger, *J. Magn. Reson.* **1982**, *50*, 485-489.
- 34** M. C. R. Symons, J. R. Morton, and K. F. Preston, in K. S. Suslick (Ed.), *High-Energy Processes in Organometallic Chemistry*, American Chemical Society, Washington, DC, 1987, pp. 169-190.
- 35** P. C. Taylor, J. F. Baugher, and H. M. Kriz, *Chem. Rev.* **1975**, *75*, 203-240.
- 36** I. V. Ovchinnikov and V. N. Konstantinov, *J. Magn. Reson.* **1978**, *32*, 179-190.
- 37** P. C. Taylor and P. J. Bray, *J. Magn. Reson.* **1970**, *2*, 305-331.
- 38** J. A. DeGray and P. H. Rieger, *Bull. Magn. Reson.* **1987**, *8*, 95-101.
- 39** B. A. Goodman and J. B. Raynor, *Adv. Inorg. Chem. Radiochem.* **1971**, *13*, 136-362.
- 40** J. R. Morton and K. F. Preston, *J. Mag. Reson.* **1978**, *30*, 577-582.
- 41** A. K. Koh and D. J. Miller, *Atom. Data Nucl. Data Tab.* **1985**, *33*, 235-253.
- 42** P. H. Rieger, *J. Mag. Reson.* **1997**, *124*, 140.
- 43** B. M. Peake, P. H. Rieger, B. H. Robinson, and J. Simpson, *J. Am. Chem. Soc.* **1980**, *102*, 156-163.
- 44** N. G. Connelly, W. E. Geiger, G. A. Lane, S. J. Raven, and P. H. Rieger, *J. Am. Chem. Soc.* **1986**, *108*, 6219-6224.
- 45** B. R. McGarvey, in T. F. Yen (Ed.), *Electron Spin Resonance of Metal Complexes*, Plenum Press, New York, 1969, pp. 1-11.
- 46** A. F. Stone, *Proc. Roy. Soc. (London)* **1963**, *A271*, 424-434.
- 47** T. Kawamura, K. Fukamachi, T. Sowa, S. Hayashide, and T. Yonezawa, *J. Am. Chem. Soc.* **1981**, *103*, 364-369.
- 48** G. A. Carriedo, V. Riera, N. G. Connelly, and S. J. Raven, *J. Chem. Soc., Dalton Trans.* **1987**,

1769-1773.

- 49** G. A. Carriedo, N. G. Connelly, E. Perez-Carreno, A. G. Orpen, A. L. Rieger, P. H. Rieger, V. Riera, and G. M. Rosair, *J. Chem. Soc., Dalton Trans.*, **1993**, 3103.
- 50** T. A. Albright, W. E. Geiger, J. Moraczweski, and B. Tulyathan, *J. Am. Chem. Soc.* **1981**, *103*, 4787-4794.
- 51** T. A. Albright and R. Hoffmann, *Chem. Ber.* **1978**, *111*, 1578-1590.
- 52** J. R. Pilbrow and M. R. Lowrey, *Rep. Prog. Phys.* **1980**, *43*, 433-495.
- 53** F. K. Kneubühl, *Phys. Kondens. Mat.* **1963**, *1*, 410-447; **1965**, *4*, 50-62.
- 54** For a summary of Kneubühl's methods, see reference 52.
- 55** W. E. Geiger, P. H. Rieger, B. Tulyathan, and M. C. Rausch, *J. Am. Chem. Soc.* **1984**, *106*, 7000-7006.
- 56** T. Lionel, J. R. Morton, and K. F. Preston, *J. Chem. Phys.* **1982**, *76*, 234-239.
- 57** S. A. Fairhurst, J. R. Morton, and K. F. Preston, *J. Chem. Phys.* **1982**, *77*, 5872-5875.
- 58** D. J. Hammack, M. M. Dillard, M. P. Castellani, A. L. Rheingold, A. L. Rieger and P. H. Rieger, *Organometallics*, **1996**, *15*, 4791.
- 59** B. M. Peake, P. H. Rieger, B. H. Robinson, and J. Simpson, *J. Am. Chem. Soc.* **1980**, *102*, 156.
- 60** B. M. Peake, P. H. Rieger, B. H. Robinson, and J. Simpson, *Inorg. Chem.* **1981**, *20*, 2540.
- 61** F. A. Cotton, J. D. Jamerson, and B. R. Stults, *J. Am. Chem. Soc.* **1976**, *98*, 1774-1779.
- 62** C. G. Howard, G. S. Girolami, G. Wilkinson, M. Thornton-Pett, and M. B. Hursthouse, *J. Chem. Soc., Dalton Trans.* **1983**, 2631-2637.